



**HAL**  
open science

## (SI) Photodissociation of vibrationally excited OH/OD radicals

David H. Parker, Gerrit C Groenenboom

► **To cite this version:**

David H. Parker, Gerrit C Groenenboom. (SI) Photodissociation of vibrationally excited OH/OD radicals. *Molecular Physics*, 2008, 106 (02-04), pp.557-572. 10.1080/00268970801922783 . hal-00513175

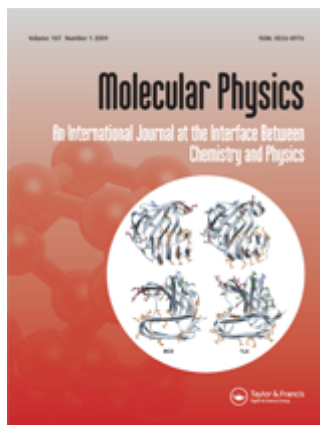
**HAL Id: hal-00513175**

**<https://hal.science/hal-00513175>**

Submitted on 1 Sep 2010

**HAL** is a multi-disciplinary open access archive for the deposit and dissemination of scientific research documents, whether they are published or not. The documents may come from teaching and research institutions in France or abroad, or from public or private research centers.

L'archive ouverte pluridisciplinaire **HAL**, est destinée au dépôt et à la diffusion de documents scientifiques de niveau recherche, publiés ou non, émanant des établissements d'enseignement et de recherche français ou étrangers, des laboratoires publics ou privés.



**(SI) Photodissociation of vibrationally excited OH/OD radicals**

Journal:	<i>Molecular Physics</i>
Manuscript ID:	TMPH-2007-0304.R1
Manuscript Type:	Full Paper
Date Submitted by the Author:	06-Dec-2007
Complete List of Authors:	Parker, David; IMM, Molecular and Laser Physics Groenenboom, Gerrit; IMM, Theoretical Chemistry
Keywords:	hydroxyl radical, photodissociation, state selection, atom polarization, sudden limit model



1  
2  
3  
4  
5  
6  
7  
8  
9 ***Photodissociation of vibrationally excited OH/OD radicals***  
10  
11  
12  
13

14 Dragana Č. Radenović, André J. A. van Roij, Shiou-Min Wu, J. J.  
15 ter Meulen, and David H. Parker<sup>1</sup>  
16

17 Molecular and Laser Physics, IMM, Radboud University Nijmegen, Toernooiveld 1,  
18 6525ED, Nijmegen, The Netherlands  
19

20 Mark P. J. van der Loo, Liesbeth M. C. Janssen and Gerrit C.  
21 Groenenboom,  
22

23 Theoretical Chemistry, IMM, Radboud University Nijmegen, Toernooiveld 1, 6525ED,  
24 Nijmegen, The Netherlands  
25  
26  
27  
28  
29  
30

31 Keywords:  
32

33 hydroxyl radical, photodissociation, state selection, atom polarization, sudden limit model.  
34  
35  
36  
37  
38  
39  
40  
41  
42  
43  
44  
45  
46  
47  
48  
49  
50  
51  
52  
53  
54  
55  
56  
57  
58  
59  
60

---

<sup>1</sup> Corresponding author: phone +31 24 3652423; fax +31 24 3653311; email [parker@science.ru.nl](mailto:parker@science.ru.nl).

**ABSTRACT**

This paper describes a joint experimental and theoretical study of the photodissociation of vibrationally excited hydroxyl radicals. OH and OD radicals produced in a pulsed electric discharge supersonic beam are state-selected and focused by a hexapole and then photo-dissociated by a single laser tuned to various H/D or O atom (2+1) resonance enhanced multiphoton ionization (REMPI) wavelengths between 243 nm and 200 nm. The angle velocity distributions of the resulting  $O^+$  and  $D^+$  photofragment ions were recorded using velocity map imaging. Photodissociation to the  $O(^3P_1) + H(^2S)$  limit is shown to take place by one-photon excitation to the repulsive  $1^2\Sigma^-$  state. The experimental data shows that vibrationally excited OH /OD which are formed in the discharge are dissociated, and a vibrational temperature of  $\sim 2000K$  was estimated for the beam source. An analysis in the high-energy recoil sudden limit is used to predict the  $O(^3P_1)$  fine structure branching ratios and alignment information in the molecular and laboratory velocity frame of the imaging experiment. The measured and predicted fine structure branching ratios and alignment parameters agree well at all dissociation wavelengths, supporting the model for photodissociation in the sudden limit regime. Several aspects of the experiment such as OH pre-alignment and orientation, ion-recoil, and Doppler-free imaging are discussed.

## 1. INTRODUCTION

Due to its central role in the photochemistry of the Earth's atmosphere, in combustion processes and in the interstellar medium, the spectra and photodynamics of the highly reactive hydroxyl radical (OH) has been the subject of numerous theoretical and experimental investigations. A wealth of detailed theoretical predictions for the photodissociation dynamics of OH is available from studies using high-quality *ab-initio* calculations of the OH electronic structure. Despite its importance, experimental studies of OH photodissociation under collision-free conditions have only recently been reported<sup>1,2</sup>.

Examination of the OH potential energy curves, Figure 1, for the optically accessible excited electronic states reveals why laboratory studies of OH photodissociation are so challenging. Given the O-H bond dissociation energy,  $D_0$ , of 4.37 eV<sup>3</sup>, photodissociation of OH can in principle occur at wavelengths shorter than 284 nm. Transitions to vibrational levels  $v' \geq 1$  of the  $A^2\Sigma^+$  state from the  $X^2\Pi$  ground electronic state, which lie in the ultraviolet (UV) region of the spectrum and are used for laser induced fluorescence detection of OH, lead to predissociation, producing  $O(^3P) + H(^2S)$  atoms. Van Dishoeck and Dalgarno<sup>4</sup> have shown that the total dissociation yield for this  $A^2\Sigma^+ \leftarrow X^2\Pi$  transition is much smaller ( $\sim 10^{-5}$ ) than photodissociation from the higher energy electronic states, thus the  $A^2\Sigma^+ \leftarrow X^2\Pi$  channel (when starting from the lowest vibrational levels of the X state) is in most circumstances of no importance in the total photodissociation process.

All of the remaining allowed electronic transitions, to the repulsive  $^2\Sigma^-$ ,  $^2\Delta$ , and  $^2\Pi$  upper states that dominate photodissociation of OH, lie in the vacuum ultraviolet (VUV) spectral region where intense laser sources are not readily available. VUV photodissociation is the main destruction process of OH in diffuse clouds in the interstellar medium, where VUV radiation is intense<sup>5,6</sup>. Besides the VUV difficulty, most sources of OH radicals also co-produce large amounts of  $O(^3P_j)$  and  $H(^2S)$  atoms, which can overwhelm the detection of photo-product signals.

1  
2 Using an electrostatic hexapole lens to concentrate and state-select our electric discharge driven OH  
3  
4 beam<sup>7</sup> in combination with the velocity map imaging detection technique<sup>8</sup>, we have succeeded in  
5  
6 observing direct photodissociation of state-selected OH/OD through the first repulsive  $1^2\Sigma^-$  state  
7  
8 under collision-free conditions, with state-specific detection of the D and O atom products<sup>1</sup>. Our OH  
9  
10 beam source<sup>7</sup> produces small amounts of vibrationally excited OH, and the internal vibrational  
11  
12 energy,  $E_{\text{vib}}$ , allows photodissociation by UV instead of VUV radiation, where  $h\nu_{\text{UV}} = h\nu_{\text{VUV}} - E_{\text{vib}}$ . Due  
13  
14 to the very low amounts of the higher vibrational states in the molecular beam, it was necessary to  
15  
16 perform a one-laser experiment, where a single laser beam is used for both photodissociation of OH  
17  
18 and detection of the O or H photo-products. This provides higher sensitivity but less flexibility than a  
19  
20 two-laser experiment. With this approach, we have carried out a series of studies of direct  
21  
22 photodissociation of OH and OD<sup>1</sup> as well as the isovalent molecules SH and SD<sup>9</sup>. A two-laser  
23  
24 dissociation-probe scheme (exciting the most populated  $X^2\Pi$  ( $v''=0$ ) level) is also being used in our  
25  
26 laboratory to study predissociation of the  $A^2\Sigma^+$  state of all four molecules. Using the high resolution  
27  
28 H atom Rydberg tagging method, Zhang and co-workers have reported  $A^2\Sigma^+$  state predissociation of  
29  
30 OH/OD<sup>2</sup> and direct UV photo-dissociation of SH/SD<sup>10</sup> and the results of these two different but  
31  
32 complementary experimental approaches are compared in this paper.

Formatted: Superscript

Deleted: 1

Deleted: 7

Formatted: English U.K.,

Formatted: English U.K.,

Deleted: 1

Deleted: 2

Formatted: English U.K.,

33  
34  
35 Our previous Communication<sup>1</sup> described photodissociation of OD radicals using velocity map  
36  
37 imaging to probe the speed and angular distribution of the  $D(^2S)$  products formed by  
38  
39 photodissociation of OD at 243 nm, and the  $O(^3P_2)$  atom products of OH/OD photodissociation at  
40  
41 226 nm. This paper describes extended studies of state-selected D ( $n=1,^2S$ ) atom detection from OD  
42  
43 at 243 nm as well as at 205 nm, along with studies of the different  $J = 2, 1, 0$  fine structure states of  
44  
45 the  $O(^3P_i)$  atoms following photodissociation of OD and OH at 226 nm and 200 nm. Doppler-free  
46  
47 imaging of OD photodissociation with D atom detection at 243 nm and ion-recoil effects in OH/OD  
48  
49 photodissociation imaging is also described. We show from experiment and first principle  
50  
51  
52  
53  
54  
55  
56  
57  
58  
59  
60

Formatted: Superscript

Deleted: 1

calculations that our images are due to one-photon dissociation to the first dissociation limit of vibrationally excited OH/OD molecules through the repulsive  $1^2\Sigma^-$  state. One-photon dissociation to the second dissociation limit, producing O( $^1D$ ) atoms, was not observed in this work, but this channel was clearly observed and characterized in the UV photodissociation of the SH and SD molecules, as reported previously<sup>9</sup>. The O( $^1D$ ) channel from OH is the subject of on-going investigation in our laboratory.

Deleted: <sup>9</sup>

Formatted: English U.K.,

## 2. PHOTODISSOCIATION OF OH

*Ab initio* potential energy curves for the ground and lower electronically excited states of OH ( $X^2\Pi, A^2\Sigma^+, 1^2\Sigma^-, 1^4\Sigma^-, 1^4\Pi, 1^2\Delta, 2^2\Pi$ ) calculated by van der Loo and Groenenboom<sup>11</sup> are presented in Figure 1. In the OH  $X^2\Pi$  ground state (Hund's case b) the  $^2\Pi_{3/2}$  spin-orbit component is  $123\text{ cm}^{-1}$  lower in energy than  $^2\Pi_{1/2}$ .<sup>12</sup> The OH  $X^2\Pi$  ground state and the  $1^2\Sigma^-, 1^4\Pi,$  and  $1^4\Sigma^-$  repulsive states correlate adiabatically with ground state product atoms O( $^3P_j$ ) + H( $n=1, ^2S$ ), while the first excited bound state  $A^2\Sigma^+$ , and the repulsive states  $1^2\Delta$  and  $2^2\Pi$  correlate with the second dissociation limit [O( $^1D_2$ ) + H( $n=1, ^2S$ )]. Van Dishoeck and Dalgarno<sup>4</sup> showed that absorption to the repulsive  $1^2\Sigma^-, ^2\Delta,$  and  $^2\Pi$  states corresponds to strong, broad bands in the VUV region of the spectrum peaking at 7.81, 9.79, and 11.25 eV, respectively. They pointed out that direct photodissociation via the  $1^2\Sigma^-$  state (which is repulsive at all distances) is the major destruction mode for OH in diffuse interstellar clouds and in comets.<sup>6</sup> Yarkony<sup>13</sup>, and others<sup>14</sup>, have predicted the final product quantum state distributions for direct dissociation and pre-dissociation of OH, which in general follow the expectations for a 'sudden limit' diabatic process. Lee<sup>15</sup>, however, predicted large deviations from the sudden limit model due to interference effects from simultaneous absorption to the repulsive wall of the  $A^2\Sigma^+$  state and the  $1^2\Sigma^-$  repulsive state. Most recently, van der Loo and Groenenboom<sup>11</sup>

Deleted: <sup>4</sup>

Formatted: Superscript

Formatted: Superscript

Deleted: <sup>6</sup>Deleted: <sup>11</sup>

Formatted: Superscript

1  
2 reported refined potential energy curves for the  $X^2\Pi$ ,  $A^2\Sigma^+$ ,  $1^2\Sigma^-$  and several high-lying Rydberg  
3  
4 states of OH, which we use in this study to explain the photodissociation dynamics of OH excited to  
5  
6 the  $1^2\Sigma^-$  excited electronic state.  
7

8  
9 The potential energy curves, position of ro-vibrational levels, transition dipole moments, *etc.*,  
10  
11 are very well determined for the OH  $X^2\Pi$  and  $A^2\Sigma^+$  electronic states. In a separate study, we will  
12  
13 report velocity map imaging of the  $O(^3P_0)$  products formed by predissociation of OH  $A^2\Sigma^+$  ( $v=3$ ,  $N=0$ ,  
14  
15 1 and 2). We have also reported two-photon resonance enhanced multiphoton ionization, (2+1)  
16  
17 REMPI, of vibrationally excited OH and OD via the  $D^2\Sigma^-$  and  $3^2\Sigma^-$  Rydberg states<sup>16</sup>. From this  
18  
19 knowledge we can state that the energies of the photons in this UV photodissociation study are not  
20  
21 resonant with any known one-photon  $A^2\Sigma^+ \leftarrow X^2\Pi(v'')$  transition, or any known two-photon  
22  
23 transitions to the  $D^2\Sigma^-$  or  $3^2\Sigma^-$  Rydberg states. In this work, photodissociation is a direct one-  
24  
25 photon process and for the photon energies used only one upper electronic state is of importance,  
26  
27 the repulsive  $1^2\Sigma^-$  state.  
28

29 As the OH  $1^2\Sigma^-$  state correlates adiabatically with the  $O(^3P_0) + H(^2S)$  limit<sup>15</sup> at the threshold for  
30  
31 photodissociation these are the only products expected. However, as seen in Figure 1, Franck-  
32  
33 Condon overlap limits absorption from the lower vibrational states of the OH  $X$  state only to excited  
34  
35 electronic states lying well above the first dissociation limit. OH photodissociation is most likely a  
36  
37 diabatic process due to this large excess energy, and due to the small mass and thus high velocity of  
38  
39 the recoiling H atom. In the diabatic picture, the electronic Hamiltonian (without spin-orbit  
40  
41 coupling) is diagonalized and spin-orbit interactions can cause coupling of the diabatic curves along  
42  
43 the dissociation coordinate. If the excess energy is much larger than the spin-orbit coupling (among  
44  
45 the  $1^2\Sigma^-$ ,  $1^4\Pi$ , and  $1^4\Sigma^-$  repulsive states) there is insufficient time for the electronic and spin angular  
46  
47 momentum to recouple at the large internuclear distance. Dissociation is then in the high-energy  
48  
49 recoil or 'sudden' limit and takes place essentially on the optically prepared diabatic state. In this  
50  
51 limit, the projection of the molecular wave function of the initial diabatic state onto the atomic basis  
52  
53  
54  
55  
56  
57  
58  
59  
60

**Formatted:** Complex Script Font:  
Bold, Superscript

**Deleted:** <sup>15</sup>

1  
2 states of the products determines the final product state distribution, and this distribution does not  
3  
4 vary with the excitation energy. The UV photodissociation of OH is considered to approach the  
5  
6 sudden limit on the diabatic  $1^2\Sigma^-$  curve.  
7

8  
9 Zhang and coworkers<sup>10</sup> studied ultraviolet photodissociation of the isovalent SH radical by  
10  
11 detecting H atom products by the high resolution Rydberg tagging time-of-flight (TOF) method. They  
12  
13 were able to resolve the three  $S^3P_J$  channels in the co-fragment H atom TOF signal, and their  
14  
15 measured J-dependent branching ratios confirm that dissociation via the  $1^2\Sigma^-$  state of SH can be  
16  
17 described using the sudden-limit approximation. While our imaging method (here applied to OH)  
18  
19 has lower velocity resolution, it can be used to detect both H and O atoms, and provides polarization  
20  
21 information ( $M_J$  state populations) for the J-state specified  $O^3P_J$  atom products. This  $O^3P_J$   
22  
23 polarization data is an important indicator of the pathways for OH photodissociation.  
24

Formatted: Superscript

Deleted: <sup>10</sup>

### 25 **3. SUDDEN LIMIT ANALYSIS OF OH PHOTODISSOCIATION**

26  
27  
28  
29

30 Potential energy curves for the  $X^2\Pi$  and  $1^2\Sigma^-$  states, reported by van der Loo and  
31  
32 Groenenboom<sup>11</sup>, are used in this section to predict the wavelength dependent photodissociation  
33  
34 cross sections for OH  $X(v'' = 0-5)$ , and their contribution in the final  $O(^3P_J)$  product distributions  
35  
36 including polarization information (as prescribed for sudden-limit dissociation) in the molecular  
37  
38 body-fixed ( $J, \omega$ ) and laboratory ( $J, M_J$ ) frame. This analysis is used later in the article for  
39  
40 interpretation of and comparison with the experimental data. A sudden limit analysis in the  
41  
42 molecular body-fixed ( $J, \omega$ ) and laboratory ( $J, M_J$ ) frame for photodissociation via the repulsive wall  
43  
44 of the  $A^2\Sigma^+$  state to the second dissociation limit was carried out in reference 9 for SH and SD. This  
45  
46 analysis is identical for OH and OD and is not repeated here.  
47

Deleted: <sup>11</sup>

Formatted: Superscript

#### 48 **3.1. Photodissociation cross sections**

49  
50  
51  
52  
53  
54  
55  
56  
57  
58  
59  
60

1  
2  
3  
4  
5  
6  
7  
8  
9  
10  
11  
12  
13  
14  
15  
16  
17  
18  
19  
20  
21  
22  
23  
24  
25  
26  
27  
28  
29  
30  
31  
32  
33  
34  
35  
36  
37  
38  
39  
40  
41  
42  
43  
44  
45  
46  
47  
48  
49  
50  
51  
52  
53  
54  
55  
56  
57  
58  
59  
60

*Ab initio* calculations of the OH/OD ground- and excited state potential energy surfaces and internuclear distance-dependent dipole transition moments are described in reference 11. Briefly, the potential energy curves and dipole transition moments are computed with MOLPRO<sup>17</sup> at the internally contracted multireference configuration interaction level<sup>18,19</sup>, with single and double excitations. Orbitals are obtained from complete active space self consistent field calculations<sup>20,21</sup>, using an aug-cc-pV6Z one-electron basis set. We use the sinc-DVR method<sup>22,23</sup> to compute the nuclear vibrational wave functions and renormalized Numerov propagation to compute the nuclear dissociative wave functions.

The  $X^2\Pi(v'')$  vibrational quantum state dependent photodissociation cross section (see Figure 1)  $\sigma$  in  $\text{cm}^2$  is given by:

$$\sigma(\omega) = \frac{4\pi^2\alpha\hbar\omega}{3e^2} \left| \langle 1^2\Sigma^-, E | \mu_x | X^2\Pi_x(v) \rangle \right|^2, \quad (1)$$

where  $\alpha$  is the fine-structure constant,  $e$  the elementary charge,  $\omega$  the frequency of the absorbed photon,  $E$  the kinetic energy release,  $\mu_x$  the x-component of the electronic dipole operator, and  $v$  the vibrational level of the ground state.

Wavelength dependent photodissociation cross sections in  $\text{cm}^2$  are plotted in the left side Figure 1 for photodissociation beginning from the OH  $X^2\Pi$   $v''=0, 2$ , and 3 vibrational states. For the OH  $X^2\Pi$  ( $v''=0$ ) state, our maximum value of  $3.15 \times 10^{-18} \text{cm}^2$  for the photodissociation cross section (at  $\sim 155$  nm) agrees well with the value of  $3.32 \times 10^{-18} \text{cm}^2$  calculated by van Dishoeck and Dalgarno.<sup>4</sup> An OH absorption cross section of  $\sim 2 \times 10^{-18} \text{cm}^2$  at 155 nm was measured by Lee and Nee<sup>24</sup> using synchrotron radiation. For our UV photodissociation wavelengths around 200 nm, the  $v''=2$  and  $v''=3$  states show local maxima while essentially no photodissociation occurs when starting from  $v''=0$ .

Formatted: Complex Script Font: 10 pt, Superscript

Deleted: <sup>4</sup>

### 3.2 Molecular and Lab frame polarization of the $O(^3P_J)$ fragment

The O atom angular distribution can be written as

$$I(\theta) \propto 1 + \beta P_2(\cos \theta), \quad (2)$$

where  $P_2$  is a second order Legendre polynomial and  $\theta$  is the angle between the laser polarization vector and the recoil velocity. In the sudden recoil limit  $\beta = -1$  for the perpendicular transition  $1^2\Sigma^- \leftarrow X^2\Pi$ . The oxygen ion image may deviate from this distribution if the  $O(^3P_J)$  atoms are polarized. The ion image angular distribution can be expanded as

$$I_j^{\text{ion}}(\theta) = p_j \sum_{k=0,2,4} c_k(J) P_k(\cos \theta) \quad (3)$$

where  $p_j$  are the fine-structure branching ratios. Expressions for the expansion coefficients

in the sudden recoil limit are given by<sup>25</sup>

$$\begin{aligned} c_0(J) &= 1 + \frac{1}{3}\beta \bar{\rho}_0^{(2)}(J)I, \\ c_2(J) &= \beta + \left(1 + \frac{2}{3}\beta\right) \bar{\rho}_0^{(2)}(J)I, \\ c_4(J) &= \beta \bar{\rho}_0^{(2)}(J)I \end{aligned} \quad (4)$$

where  $\bar{\rho}_0^{(k)} = \rho_0^{(k)}(J)/\rho_0^{(0)}$ . The rank  $k$  irreducible components of the density matrix

Formatted: English U.S.

Field Code Changed

Formatted: English U.S.

Field Code Changed

Formatted: English U.S.

1  
2  
3  $\rho_0^{(k)}$  are related to the populations  $p_{J\omega}$  of the molecule-fixed fine-structure states of the oxygen  
4  
5 fragment, through  
6  
7

$$\rho_0^{(k)} = \sum_{\omega=-J}^J (-1)^{J-\omega} \langle J, \omega, J, -\omega | k 0 \rangle \quad (5)$$

8  
9  
10  
11  
12  
13  
14 where  $\langle J, \omega, J, -\omega | k 0 \rangle$  are Clebsch-Gordan coefficients. The relative absorption intensities  $I_2(J)$  for

15  
16  
17  
18  
19  
20  
21 the (2+1) REMPI oxygen detection scheme as defined by Mo *et al.*<sup>26</sup> are  $I_2(1) = 1/\sqrt{2}$  and  $I_2(2) =$

22  
23  
24 (ref 25). In the above equations we already substituted  $I_4(2) = 0$ .

25  
26  
27  
28 In the sudden recoil limit the populations  $p_{J\omega}$  are computed by expanding the  $1^3\Sigma^-$  molecular

29  
30  
31  
32  
33  
34 basis  $|A = 0, S = 1/2\rangle$  excited state in the product atomic basis  $|S_H = 1/2, \sigma_H | J\omega \rangle$ <sup>25,27</sup>. Here  $\Sigma$

35  
36  
37  
38  
39  
40  
41  
42 is the projection of the molecular spin onto the interatomic axis. Since the H atom is in an S-state,

43  
44  
45  
46 we only require the H-atom spin wave function  $|S_H \sigma_H \rangle$  and the orbital part of the  $O(^3P)$  oxygen

atom is given by  $|\Lambda\rangle$ , with  $L = 1$ . The spin part of the molecular wave function can be written as the

coupling of the H-atom spin function and the O-atom spin function  $|\Sigma\rangle$ ,

$$|\Sigma\rangle = \sum_{\sigma_H \sigma_O} |S_H \sigma_H\rangle |S_O \sigma_O\rangle \quad (6)$$

The uncoupled O-atom wave function may be expanded in fine-structure states through

$$|\Lambda\rangle |S_O \sigma_O\rangle = \sum_{j=0}^2 \sum_{\omega=-j}^j |J\omega\rangle \langle \Lambda S_O \sigma_O | J\omega\rangle \quad (7)$$

Combining the last two equations gives

$$|\Lambda\Sigma\rangle = \sum_{\omega} |J\omega\rangle \langle S_H \sigma_H | J\omega\rangle \langle S_H \sigma_H S_O \sigma_O | \Sigma\rangle \langle \Lambda S_O \sigma_O | J\omega\rangle \quad (8)$$

and we find for the molecular state  $1^2\Sigma^-$ , with  $\Lambda = 0$ , and  $S = 1/2$  and  $|\Omega| = |\Sigma| = 1/2$ , in

the sudden recoil limit

$$p_{J\omega} = \frac{1}{2} \sum_{\Omega=\pm 1/2} |\langle S_H, \Omega - \omega, S_O, \omega | \Sigma\rangle \langle \Lambda S_O \omega | J\omega\rangle| \quad (9)$$

The fine-structure branching ratios for the oxygen atoms are given by  $p_J = \frac{P_J}{\sum_J P_J}$ . The

branching ratios for the ions, i.e., taking into account the polarization effects are given by

$$r_J = \frac{P_J \beta_J}{\sum_J P_J \beta_J}. \quad (10)$$

The fine-structure populations and the Legendre moments of the normalized ion images,  $\beta_J = c_2(J)/c_0(J)$  and  $\gamma_J = c_4(J)/c_0(J)$  are given in Table 1. There are, for example, no projections possible of the  $^2\Sigma^-$  electronic state ( $\Omega = 1/2$ ) onto a final state configuration of  $H(^2S_{1/2})$  and  $O(^3P_2)$  ( $\Omega = 5/2, 3/2$ ). Inspection of Table 1 shows that the  $O(^3P_{J=2:1:0})$  fine-structure branching ratios are the same as the statistical 5:3:1 pattern, but the distributions  $p_{J\omega}$  for a given J value are far from statistical. The branching ratios  $r_J$ , that are obtained from integrating the angular distributions and that take into account the polarization effects, deviate slightly from the atomic branching ratios  $p_J$ . Note that the  $J=0$   $O(^3P_0)$  product atom shows the expected  $\beta = -1$  for a  $\Sigma \leftarrow \Pi$  excitation, while  $J=1$  and 2 have  $\beta < -1$  and significant (negative)  $\gamma$  values.

#### 4. EXPERIMENTAL METHOD

1  
2  
3  
4  
5  
6  
7  
8  
9  
10  
11  
12  
13  
14  
15  
16  
17  
18  
19  
20  
21  
22  
23  
24  
25  
26  
27  
28  
29  
30  
31  
32  
33  
34  
35  
36  
37  
38  
39  
40  
41  
42  
43  
44  
45  
46  
47  
48  
49  
50  
51  
52  
53  
54  
55  
56  
57  
58  
59  
60

Our velocity map imaging apparatus has been described in detail elsewhere<sup>1, 16</sup> thus only a summary of the experimental details concerning the molecular beam and hexapole state selector will be given here. Two differentially pumped vacuum chambers are used: one chamber for the production of OH/OD molecules and the other chamber for the state selection of OH/OD photodissociation, and detection of one of the fragments from OH/OD. The source chamber is pumped by a diffusion pump and the detection chamber is differentially pumped by a turbo pump with additional pumping by a liquid N<sub>2</sub>-cold trap. The OH/OD beam source was produced by a mixture of H<sub>2</sub>O/D<sub>2</sub>O molecules seeded in Ar as the carrier gas. The mixture is prepared by bubbling Argon at a backing pressure of 1.5 bar through liquid water at room temperature (vapor pressure of 24 mbar). For the expansion a Jordan pulsed valve with a 0.4 mm diameter nozzle is used, which is mounted along the direction of the time of flight tube. The OH/OD radicals are produced by dissociation of H<sub>2</sub>O/D<sub>2</sub>O at the beginning of the expansion by an electrical discharge between a stainless steel ring (4 mm diameter, 0.5 mm thick) and the grounded valve body<sup>7</sup>. The ring, which is located on-axis 2.5 mm from the nozzle, is pulsed (20 μsec, 2 kV) to negative high voltage during the ~60 μsec expansion.

After their production, the electrically neutral OH/OD molecules cool down to the ground rotational level of each vibrational state in the supersonic expansion and pass through a 1 mm diameter skimmer which separates the source and detection chambers. The skimmer is positioned 15 mm from the nozzle. The cold molecular beam enters a 120 mm long hexapole state selector 50 mm downstream of the nozzle, which focuses OH/OD in the  $\Omega=3/2$ ,  $J=3/2$ ,  $|M_J| = 3/2, 1/2$  states in the upper  $\Lambda$ -doublet of  $f$ -symmetry<sup>28</sup> to the laser interaction region between the repeller plate and the extractor plate of the electrostatic lens. The hexapole is constructed with 3 mm cylindrical rods and has an inner diameter of 6 mm. The distance from the entrance of the hexapole to the valve and the distance from the exit of the hexapole to the collision center is 50 mm. The total distance between the valve and the collision zone is 220 mm. The enlargement of the distance between the

Formatted: Superscript

Deleted: <sup>1</sup>Deleted: <sup>17</sup>

1  
2 source and photodissociation area by the insertion of the state selector decreases the contributions  
3  
4 from all other species in the discharge beam, while the hexapole increases the concentration of the  
5  
6 state-selected component by a factor of  $\sim 8$  at the crossing point with the photodissociation laser.  
7

8  
9 Using both laser induced fluorescence (LIF) and resonance enhanced multiphoton ionization  
10 (REMPI) detection techniques<sup>29,30</sup> the only species in the beam that was found to focus with the  
11 hexapole was OH/OD. A corresponding increase in signal for the photodissociation processes with  
12 the hexapole 'on' is thus direct proof that the photodissociation signal arises from OH/OD. The UV  
13 laser beam propagates perpendicular to the molecular beam and is focused with a 200 mm focal  
14 length lens, and has its electric field polarization direction lying parallel to the detector face. In our  
15 experiments only one laser is used, both for dissociation of the OH/OD and detection of one of the  
16 fragments  $O(^3P_{2,1,0})$  from OH,  $O(^3P_{2,1,0})$  from OD or  $D(^2S)$  from OD. There was too much apparatus  
17 background to detect H from OH. The laser wavelength is chosen for two-photon resonant three-  
18 photon ionization [(2+1) REMPI] of either the  $O(^3P_{2,1,0})$  atom products at  $\sim 226$  nm and  $\sim 200$  nm<sup>31</sup> or  
19 the  $D(^2S)$  atom products at  $\sim 243$  nm and  $\sim 205$  nm. We find that the relative sensitivity for all three  
20  $O(^3P_j)$  states at  $\sim 200$  nm is similar and that the overall sensitivity is a factor of  $\sim 7$  lower than at  $\sim 226$   
21 nm for similar experimental conditions.  
22  
23  
24  
25  
26  
27  
28  
29  
30  
31  
32  
33

34 UV laser light of  $\sim 2$  mJ/pulse was generated by frequency doubling the output of a dye laser  
35 (Continuum TDL60) for  $\sim 226$  nm (Coumarin 47 dye) and  $\sim 243$  nm (Coumarin 102 dye). In the 200-  
36 205 nm region  $\sim 1$  mJ/pulse was generated by frequency tripling the output of a dye laser (Spectra  
37 Physics Quanta Ray PDL-2) operating with a mixture of Sulforhodamine B and Rhodamine 640. Ions  
38 created in the laser-molecular beam intersection area are extracted and rapidly accelerated into the  
39 time-of-flight region by an electrostatic velocity mapping lens consisting of a 100 mm diameter  
40 repeller, extractor, and ground plates separated by 15 mm. The repeller electrode has a 4 mm center  
41 opening and the other two lenses have openings of 20 mm. At the end of the TOF tube the ions  
42 strike a position sensitive detector, which consists of two microchannel plates (MCP) followed by a  
43  
44  
45  
46  
47  
48  
49  
50  
51  
52  
53  
54  
55  
56  
57  
58  
59  
60

1  
2 P-20 phosphor screen. Mass selectivity was achieved by pulsing on the gain of the detector as the  $D^+$   
3 or  $O^+$  ions arrive. The 2-D images on the phosphor screen are recorded with a CCD camera and  
4 stored in a PC where further data analysis is performed.  
5  
6  
7  
8

## 9 **5. EXPERIMENTAL RESULTS AND ANALYSIS**

### 10 **5.1. General description of the images**

11  
12  
13  
14  
15  
16 A set of raw photofragment images of  $O(^3P_J)$  photofragments from the photo-dissociation of OH  
17 and OD, and  $D(^2S)$  photofragments from the photodissociation of OD are shown in Figure 2. These  
18 images are 2D projections of the 3D velocity distributions with the polarization vector of the  
19 photodissociation laser beam maintained parallel to the detector face and thus along the vertical  
20 axis of the figure. All of the images show a strong spot in the middle of the image which corresponds  
21 to  $O(^3P_J)$  or  $D(^2S)$  atoms formed in the discharge and cooled in the expansion.  
22  
23  
24  
25  
26  
27

28  
29 State-selective detection of  $O(2p^4\ ^3P_J)$  is achieved either by two-photon resonant, one-photon  
30 ionization ((2+1) REMPI) through the  $O(2p^33p^1, \ ^3P_J)$  states using the vacuum wavelengths of 225.654,  
31 226.059 and 226.233 nm for  $J = 2, 1, 0$ , respectively or by (2+1) REMPI through the  $O(2p^34p^1, \ ^3P_J)$   
32 states using the vacuum wavelengths of 200.640, 200.959 and 201.097 nm for  $J = 2, 1, 0$ ,  
33 respectively. State-selective detection of  $D(1s\ ^2S)$  is achieved either by (2+1) REMPI through the  
34  $D(2s\ ^2S)$  state using the vacuum wavelengths 243.09 nm or by (2+1) REMPI through the  $D(3s\ ^2S)$   
35 states using 205.07 nm. The images shown in Figure 2 are calibrated using  $O(^3P_2)$  from the  
36 photodissociation of  $O_2$  at  $\sim 226$  nm and by  $D(^2S)$  from DI photodissociation at  $\sim 243$  nm. The radius of  
37 the ring is proportional to the velocity of the products, so after calibration at one radius the kinetic  
38 energy release corresponding to all other rings is determined. At least 2 rings are seen in each image  
39 in Figure 2, each with a perpendicular ( $\sim \sin^2\theta$ , with  $\theta = 0^\circ$  defined at the top center axis of the  
40 image) angular distribution. An overview of the velocity information extracted for each observed  
41  
42  
43  
44  
45  
46  
47  
48  
49  
50  
51  
52  
53  
54  
55  
56  
57  
58  
59  
60

1  
2 ring is presented in Table 2. As required from momentum balance, the O images from OD  
3  
4 photodissociation are larger (in the proper ratio) than those from OH photodissociation at the same  
5  
6 energy, which is an additional proof that the images originate from OH/OD.  
7

8  
9 Raw (hexapole on-off)  $O(^3P_1)^+$  images produced by photodissociation of OH and OD at  $\sim 226$  nm  
10 are presented in Fig. 2a) and b), respectively, and a raw  $D(^2S)^+$  image (hexapole on-hexapole off)  
11 produced by photodissociation of OD at  $\sim 243$  nm is presented in Fig. 2c). All of these images are  
12 summations of 50000 laser shots. The background-induced signal at the center of the images is not  
13  
14 fully eliminated by the hexapole on-off subtraction scheme, causing a slight overload of the CCD  
15  
16 camera at this position, especially for the  $O(^3P_2)$  images. Raw  $O(^3P_1)$  images for photodissociation of  
17  
18 OH and OD at  $\sim 200$  nm which are taken using event counting and only with the hexapole 'on' are  
19  
20 shown in Fig. 2a') and b'), respectively. In Fig. 2c') a raw (hexapole on-hexapole off)  $D(^2S)^+$  image  
21  
22 produced by photodissociation of OD at  $\sim 205$  nm is presented. The  $O^+$  images from OH are  
23  
24 summations of 90 000 laser shots, and the  $O^+$  and  $D^+$  images from OD are summations of 230 000  
25  
26 laser shots.  
27  
28

29  
30 Direct detection of  $O(^1D_2)$  products from the dissociation of OD using (2+1) REMPI via the  $^1P_1$   
31 state at 205.473 nm (vac.) was also attempted. While a small signal at the center of the image from  
32  
33  $O(^1D)$  produced in the discharge was observed, we did not observe any convincing  $O(^1D)$  signal from  
34  
35 the photodissociation of OD at 205 nm.  
36  
37

## 38 39 **5.2. $O(^3P_1)$ branching ratios**

40  
41  
42

43  
44 Experimental branching ratios for the channels  $[O(^3P_2) + H(^2S)]: [O(^3P_1) + H(^2S)]: [O(^3P_0) + H$   
45  
46  $(^2S)]$  of OH and  $[O(^3P_2) + D(^2S)]: [O(^3P_1) + D(^2S)]: [O(^3P_0) + D(^2S)]$  of OD at  $\sim 226$  and  $\sim 200$  nm are  
47  
48 given in Table 3. The total OH photodissociation signal strength was determined for each raw image  
49  
50 at constant laser pulse energy. For these one-laser experiments, the dissociation and detection laser  
51  
52  
53  
54  
55  
56  
57  
58  
59  
60

polarization are the same, and set parallel to the imaging detector plane. No corrections were made for the effects of the fixed (linear) laser polarization on the total detection sensitivity. A simulation of the experiment using the sudden-limit values from section 3 predicts a <5% deviation between a polarized and non-polarized detection laser, which is less than our experimental uncertainty.

### 5.3. Velocity and Kinetic Energy Analysis and Assignment of the images

Velocity and kinetic energy data is presented in Table 2. The two main rings seen in the  $O(^3P_J)$  images (Fig. 2a) arising from photodissociation of OH at ~226 nm, for example, have a velocity of 1200 and 1300 m/s, respectively, with an uncertainty in the peak position ( $\Delta v$ ) of +/-20 m/s.

Converting these velocities to total kinetic energy release [TKER =  $(m_{OH} / m_H) \times KER_O (= \frac{1}{2} m_O v_O^2)$ ] yields values of 2.02 and 2.39 +/-0.06 eV, respectively. TKER for O atoms from OD photodissociation =  $(m_{OD} / m_O) \times KER_O$  and for D atoms from OD TKER =  $(m_{OD} / m_D) \times KER_D$ .

Kinetic energy distributions were obtained from the inversion of raw images using the BASEX program<sup>32</sup>, which assumes cylindrical symmetry about the dissociation laser polarization in the experiment. Possible deviations from cylindrical symmetry due to the state-selection of the molecular beam are discussed in section 5.8. The effects of product atom alignment were accounted for in the theoretical analysis of section 3. Vertical sections through the 3-D distribution of two representative inverted images of O ( $^3P_2$ ) and D ( $^2S$ ) from the photodissociation of OD at 200 and 205 nm, respectively are shown in Fig. 3a) and b).

The corresponding kinetic energy distributions from these reconstructed images, extracted by integrating over all angles, are shown in Fig. 4. Weak signals due to OH are seen at lower kinetic

Deleted: 3

Formatted: Font: Symbol

energy in the  $O(^3P_2)$  from OD image. The reconstructed images from  $O(^3P_2)$  REMPI at  $\sim 226$  and  $\sim 200$  nm arising from the photodissociation of OH are shown in Fig. 5, and the corresponding TKER curves obtained from integrating over the angular distribution of the inverted images are shown in Fig. 6. A beam vibrational temperature is estimated from the relative peaks heights in the kinetic energy distributions.

Each peak in the kinetic energy distribution can be assigned using the energy balance equation  $TKER = hv + E(vib)_{OH/D} - D_0(OH/OD)$ , with the bond energy of OH/OD,  $D_0(OH/OD)$ , from references 3, 33, and 34, and the recently calculated vibrational energies for ground  $X^2\Pi$  state of OH/OD,

$E(vib)_{OH/D}$ , from Loo and Groenenboom<sup>11</sup>. Complementary first principle calculations (Fig. 1.) confirm that one-photon excitation of OH/OD  $X^2\Pi(v'')$  to the repulsive  $1^2\Sigma^-$  curve has a reasonably strong ( $\sigma_{max} > 10^{-20} \text{ cm}^2$ ), wavelength-dependent photodissociation cross section in the 200-250 nm region.

The two main rings seen for  $O(^3P_1)$  atom detection at 226 nm in Fig. 2a, for example, attributed in Table 2 to photodissociation of OH in vibrational levels  $v'' = 2$ , and 3, have photodissociation cross sections of  $\sim 6.45 \times 10^{-20} \text{ cm}^2$  and  $\sim 3.22 \times 10^{-19} \text{ cm}^2$ , respectively. Depending on the dissociation/detection wavelength and the molecule (OH or OD), excitation of the OH  $X(v'')$   $v'' = 1-4$  states are observed. We should point out that the vibrational energy of OH( $v'' = 3$ ) is  $10199.39 \text{ cm}^{-1}$ , which for a molecular beam temperature of  $\sim 2000\text{K}$  (see next section) has a population probability of only  $2 \times 10^{-5}$ .

#### 5.4. Temperature of the discharge beam

The relative intensity of the peaks observed in the TKER curves of Figs. 3 and 5 can be qualitatively understood using the photodissociation cross sections computed for each OH  $X(v'')$  vibrational state (Fig. 1). The relative peaks heights determined from the  $O(^3P_2)$  and  $D(^2S)$  fragment atoms images for the higher energy regime,  $\sim 200$  and  $\sim 205$  nm, respectively, were found to agree with calculated photodissociation yields for an OD molecular beam with a vibrational temperature of

Formatted: Superscript

Formatted: Subscript

Deleted: <sup>11</sup>

Formatted: Superscript

1  
2 2000 K. While in our previous study<sup>1</sup> a vibrational temperature of  $\sim 1700$  K was estimated, a  
3  
4 vibrational temperature of 2000 K agrees better with the present, more extensive, experimental  
5  
6 data. The effect of an electric discharge on the vibrational excitation, relaxation, and energy  
7  
8 transfer of diatomic molecules in pulsed supersonic beams has been the subject of several previous  
9  
10 studies<sup>35, 36, 37, 38</sup>. The final vibrational temperature of a pulsed discharge has been found to depend  
11  
12 on a large number of experimental parameters, including backing pressure, buffer gas, discharge  
13  
14 condition and geometry of the nozzle. Our experimental value compares reasonably with other  
15  
16 studies of discharge sources. A discharge of NO in He produced an NO vibrational temperature of  
17  
18 6500K, for example<sup>37</sup>, while a similar discharge<sup>38</sup> in OCS produced an SO vibrational temperature of  
19  
20  $\sim 1000$ K.

Deleted: <sup>1</sup>Formatted: Font: 11 pt, Complex  
Script Font: 11 pt, SuperscriptDeleted: <sup>37</sup>Formatted: Font: 11 pt, Complex  
Script Font: 11 pt, SuperscriptFormatted: Font: 11 pt, Complex  
Script Font: 11 pt, SuperscriptDeleted: <sup>38</sup>

21  
22  
23  
24 At a vibrational temperature of 2000K, the  $v''=1-3$  states of OH contains only 5, 0.3, and 0.002%  
25  
26 of the total population. The sensitivity of the imaging experiment is thus quite high in order to  
27  
28 image the neutral photodissociation products from such small fractions of the beam population. In  
29  
30 our previous 2+1 REMPI study<sup>16</sup> of OH we were able to detect transitions from the ( $v''=1,2,3$ )  
31  
32 vibrationally excited states to the higher lying  $D^2\Sigma^-$  and  $3^2\Sigma^-$  Rydberg states. We did not observe  
33  
34 any (2+1) REMPI transitions from vibrational levels higher than  $v''=3$ . Our previous study used the  
35  
36 same OH source as in the present study and the REMPI spectra also confirmed that the OH radicals  
37  
38 produced in the discharge source are indeed vibrationally hot, but rotationally quite cold ( $<20$ K). The  
39  
40 population in the excited rotational states is effectively relaxed in the supersonic expansion due to  
41  
42 the relatively small rotational spacing but the vibrational spacing is too large to allow an efficient  
43  
44 relaxation.

### 45 46 **5.5. Ion recoil effects on kinetic energy resolution**

47  
48  
49  
50  
51  
52  
53  
54  
55  
56  
57  
58  
59  
60

1  
2 While ion recoil<sup>39,40,41</sup> is deleterious in both O atom and D atom imaging, the O atom kinetic  
3 energy resolution is most affected, as is evident in the curves shown in Figure 4. Photodissociation of  
4 a state-selected diatomic molecule should lead to sharp peaks in the KER curves, while the observed  
5 peaks are quite broad. In our previous OH photodissociation study<sup>1</sup> we pointed out that the velocity  
6 resolution is limited by ion recoil from the (2+1) REMPI detection process. The large excess  
7 ionization energy ( $3h\nu-IP$ ) when partitioned by momentum conservation creates a high velocity  
8 electron and low, but non-zero, velocity fragment ion. This effect is most important for combined  
9 photodissociation and REMPI detection using the higher energy  $\sim 200$  and  $\sim 205$  nm photons. On  
10 conversion of the neutral fragments to ions, the ion recoil, a fixed and known velocity sphere, is  
11 added to the original velocity vector of the neutral  $O(^3P_j)$  and  $D(^2S)$  photofragments. While the  
12 added ion-recoil velocity is relatively small, it causes significant broadening when its magnitude  
13 approaches the velocity spacing of neighboring rings in the image. The percentage effect of ion  
14 recoil on the velocity of the nascent O or D fragment is roughly independent of the fragment mass  
15 because a higher mass atom (O from OH/OD) has a lower nascent velocity due to the mass  
16 partitioning factor in the TKER equation.

17  
18 In order to quantify the O atom ion recoil we have measured an  $O^+$  image of cold (zero  
19 transverse velocity)  $O(^3P_2)$  atoms created in the discharge beam. A magnification lens similar to that  
20 of reference 42 was used to magnify the image of low velocity  $O^+$  to observe the ion-recoil effect.  
21  $O(^3P_2)$  ion-recoil is characterized as a mixed perpendicular angular distribution ( $\beta \sim -0.2$ ), which  
22 causes significant broadening of the O/D atom signal, especially along  $\theta=90^\circ$ , where  $\theta$  is the angle  
23 between the recoil velocity vector and the polarization direction of the linearly polarized REMPI  
24 laser. This anisotropic broadening is added to each velocity component of the perpendicular  
25 ( $\Sigma \leftarrow \Pi$ ) angular distribution.

26  
27 The two-photon excited  $n=2$  s electron in the (2+1) REMPI of  $D(^2S)$  atoms at  $\sim 243$  and  $\sim 205$  nm  
28 is ejected as a  $p$  wave, thus with a pure parallel or  $\cos^2\theta$  distribution. This causes an observable  
29  
30  
31  
32  
33  
34  
35  
36  
37  
38  
39  
40  
41  
42  
43  
44  
45  
46  
47  
48  
49  
50  
51  
52  
53  
54  
55  
56  
57  
58  
59  
60

Formatted: Font: 11 pt, Complex  
Script Font: 11 pt, Superscript

Deleted: <sup>1</sup>

splitting of the rings in the regions of from  $0 < \theta < 45^\circ$  and blurring of the rings around  $\theta = 90^\circ$ , where most of the signal lies. It is possible to decrease the recoil blurring by using slicing methods<sup>43</sup> and by setting the probe laser polarization direction perpendicular to the detector face.

The ion recoil velocity (Table 2) for O and D atom detection at the employed wavelengths should be compared with the photofragment velocity. In the case of (2+1) REMPI of  $O(^3P_j)$  atoms at  $\sim 226$  nm, for example, the three-photon energy is 16.47 eV while the O atom ionization potential is 13.62 eV. The total excess kinetic energy is 2.9 eV, which is subdivided between the electron and  $O^+$  ion according to the mass ratios, i.e.  $KER(O^+) = (m_e/m_o) * TKER$  ( $m_e = 5.5 \cdot 10^{-4}$  amu), yielding  $v_{recoil O^+} = 35$  m/s. The shifts in velocity for the rings observed in this study vary over the range of  $\pm 1.7\%$  to  $\pm 3.6\%$ . More important is the relative peak spacing of the rings compared to the ion recoil. Since the recoil adds in all directions, photodissociation of the OH  $v''=2$  and 3 molecules at 226 nm, for example, yields O atom peaks along  $\theta=90^\circ$  that are shifted closer to each other by 70 m/s, compared to their original spacing of 118 m/s. Other apparatus effects, particularly space charge and the transverse velocity spread of the parent OH beam, produce further broadening of the peaks.

### 5.6. Angular distributions

Angular distributions,  $I(\theta)$ , were obtained by integrating the inverted image over the velocity range (which includes the ion-recoil spreading) of each ring. These are fitted to the expression:  $I(\theta) \sim 1 + \beta P_2(\cos \theta) + \gamma P_4(\cos \theta)$  where  $P_2(\cos \theta)$  and  $P_4(\cos \theta)$  are the second- and fourth-order Legendre polynomials, respectively, and  $\beta$  and  $\gamma$  are anisotropy parameters. In the absence of alignment in the probed fragment, the anisotropy parameter  $\beta$  ( $-1 \leq \beta \leq +2$ ) is  $-1$  for a pure perpendicular transition and  $+2$  for a pure parallel transition. These extreme values of  $\beta$  can only be obtained if the dissociation lifetime  $\tau$  of the excited state is much shorter than the rotation period,  $\tau_{rot}$ , of the parent molecule (direct axial dissociation). In the absence of product atom alignment ( $O^3P_0$  and  $D^2S$  products) the anisotropy parameter  $\gamma = 0$ . When atomic alignment is present and probed by the

Deleted: T

Deleted: ic

1  
2 linearly polarized REMPI laser, both  $\beta$  and  $\gamma$  are necessary to fit the angular distributions, as is  
3  
4 described in the sudden limit analysis.  
5  
6  
7

8  
9 A perpendicular transition from the ground  $X^2\Pi$  state to the directly dissociative  $1^2\Sigma^-$  electronic  
10 state should yield  $\beta = -1$ . As is obvious from Fig. 2, all of the observed angular distributions are  
11 roughly perpendicular. For the stronger rings in the  $D(^2S)$  atom images for photodissociation of OD  
12 at  $\sim 243$  and also at  $\sim 205$  nm, an almost fully perpendicular angular distribution is observed. As  
13 discussed in the next section, a fully perpendicular angular distribution ( $\beta = -1$ ) for photodissociation  
14 of OD at  $\sim 243$  nm was measured for the strongest ring in the  $D^+$  image by applying Doppler-free  
15 (2+1) REMPI, which is less sensitive to background D atoms than standard (2+1) REMPI.  
16  
17  
18  
19  
20  
21  
22  
23  
24

25 Representative angular distributions for the strongest peaks of the dissociation products  
26  $O(^3P_{2,1,0})$  from OH/OD at 226 and 200 nm and  $D(^2S)$  from OD at 243 and 205 nm are shown in Fig. 7.  
27 Anisotropy parameters  $\beta$ ,  $\gamma$  determined from the angular distribution of  $O(^3P)$  fragments are given in  
28 Table 4. The estimated uncertainty of  $\beta$  and  $\gamma$  is typically 0.1. Uncertainty values of  $\beta$  or  $\gamma$  exceeding  
29 0.1 are indicated in the table. It is clear from Table 4 that the fine-structure dependent  $\beta$   
30 parameters at 226 and 200 nm deviate strongly from  $-1$  for  $O(^3P_{2,1})$ . Alignment of the  $O(^3P_{2,1})$   
31 photofragments is observed as a dip in signal strength (corresponding to a negative  $\gamma$  value) along  
32 the  $\theta = 90^\circ$  in the image.  $\beta$  becomes more negative as the angular momentum  $J$  of the  $O(^3P_J)$   
33 photofragments decreased and the value of the anisotropy parameter  $\gamma$  increases with the  
34 decreasing values of  $\beta$  over the fine structure levels. These trends are predicted by the sudden limit  
35 analysis in section 3.  
36  
37  
38  
39  
40  
41  
42  
43  
44  
45  
46

47 In Figure 8 the anisotropy parameters  $\beta$  and  $\gamma$  from Table 4 are plotted as a function of  
48 dissociation wavelength. It can be seen from this figure that the anisotropy parameters of the three  
49  $O(^3P_J)$  channels are different from each other, but there are no large variations in these parameters  
50  
51  
52  
53  
54  
55  
56  
57  
58  
59  
60

1  
2 (within the experimental error limit) as a function of excitation energy at  $\sim 226$  and  $\sim 200$  nm. There  
3  
4 is also no significant variation in the  $\beta$  parameter for D atoms from OD photodissociation at 243 nm  
5  
6 compared to 205 nm.  
7

### 8 9 **5.7. Doppler-free Imaging**

10  
11  
12  
13 Another origin of ring broadening is space charge, which occurs when the laser-created ion  
14  
15 density is too large. On increasing the laser power as much as possible to obtain a reasonable  
16  
17 photofragment signal we also ionize non-signal species which further increases space charge. To  
18  
19 decrease this effect and also avoid errors in scanning over the Doppler profile when taking the  
20  
21 image, we apply the Doppler-free (2+1) REMPI<sup>44</sup> to probe the D atom products from  
22  
23 photodissociation of OD. In our configuration we used two counter-propagating linearly polarized  
24  
25 laser beams to ionize the D(1s <sup>2</sup>S) atoms by (2+1) REMPI through the D(2s <sup>2</sup>S) state at the center  
26  
27 wavelength of 243.09 nm. The laser light at 243.09 nm ( $\sim 1.5$  mJ/pulse, 5 ns pulse length,  $0.4$  cm<sup>-1</sup>  
28  
29 bandwidth) is tuned to the center of the Doppler profile and focused with a 20 cm lens onto the  
30  
31 molecular beam. The laser beam was retro-reflected with a 25 cm focal length spherical mirror and  
32  
33 refocused onto the molecular beam. The polarization vector of the both beams was parallel to the  
34  
35 detector face. Note that this configuration is not optimal, there is a 50 cm ( $\sim 2$  ns) delay between the  
36  
37 two beams, and the laser bandwidth is also much broader than desired for optimal Doppler-free  
38  
39 detection. When the two beams overlap spatially the total signal increased by a factor of  $\sim 15$ , which  
40  
41 allowed the use of lower laser power and thus resulted in less space charge and background effects.  
42  
43 The Doppler-free condition ensures detection of all velocity components with equal sensitivity, but  
44  
45 the two single-beam signals which are always present strongly favor detection of the zero velocity  
46  
47 atoms from the discharge, which appear in the center of the image. The D atom Doppler-free signal  
48  
49 is not disturbed by the zero velocity signals in the middle of the image.  
50  
51  
52  
53  
54  
55  
56  
57  
58  
59  
60

1  
2 The Doppler free raw image of  $D(^2S)$  and the corresponding slice through the inverted 3-D image  
3  
4 are presented in Fig. 9. By this method a pure perpendicular angular distribution was measured for  
5  
6 the strongest ring in D atom image ( $\beta = -1.0 \pm 0.1$ )  
7

### 8 9 **5.8. Effect of parent molecule orientation and alignment**

10  
11 Our experimental conditions, *i.e.*, a molecular beam passing through a hexapole state selector  
12  
13 into a static electric field, are similar to those used for studies of the photodissociation of oriented  
14  
15  $CH_3I$  molecules<sup>45</sup> or orientation effects in OH inelastic collisions<sup>46</sup>. On exiting the hexapole the *f*-state  
16  
17 selected OH molecules ( $\Omega=3/2$ ,  $J=3/2$ ,  $M_J=3/2, 1/2$ ) fly 5 cm before passing through a 4 mm hole in  
18  
19 the center of the repeller plate electrode, which is biased typically at -3000V. Due to this large  
20  
21 repeller plate opening and single hexapole configuration we estimate that at about 60% of the OH  
22  
23 molecules studied are in the  $M_J=1/2$  state. Within the imaging lens, at the point where  
24  
25 photodissociation and photoionization takes place, the static field is  $\sim 710$  V/cm. While this is a  
26  
27 rather low field, it causes parity mixing of the *e* and *f* levels and a slight pre-orientation of the state-  
28  
29 selected OH<sup>46</sup>. Parity mixing is observable in the REMPI and LIF spectra of the state-selected OH,  
30  
31 and can be avoided by pulsing on the velocity mapping field after laser excitation and ionization has  
32  
33 taken place. Pre-orientation of the  $M_J=1/2$  state is negligible at 710 V/cm, and pre-orientation of the  
34  
35  $M_J=3/2$  state caused by this field is not observable in a photodissociation process because the  
36  
37 orientation field is parallel with the ion TOF direction. Information mapped along the TOF direction  
38  
39 is lost in the 'crush' of the 3D image onto the 2D detector. Our OH sample used for  
40  
41 photodissociation imaging is thus effectively isotropic within our data uncertainties, which means we  
42  
43 can assume cylindrical symmetry around the laser polarization direction in order to analyze the raw  
44  
45 images using standard inversion procedures (Basex program)<sup>32</sup>.

Formatted: English U.K.,

Deleted: 45

Deleted: 32

Formatted: English U.K.,

## 46 47 **6. DISCUSSION**

48  
49  
50  
51  
52  
53  
54  
55  
56  
57  
58  
59  
60

1  
2 Experimentally observed  $O(^3P_j)$  fine structure branching ratios and angular distribution  
3  
4 parameters ( $\beta$ ,  $\gamma$ ) for OH/OD photodissociation in the UV region are presented in Tables 3 and 4  
5  
6 respectively, and the angular distribution data is plotted in Figure 8 along with the calculated  
7  
8 sudden-limit values given in Table 1. Within the error limits of the experiment, both the branching  
9  
10 ratios and polarization sensitive angular distribution parameters agree with the calculated sudden-  
11  
12 limit values for OH and OD at each dissociation wavelength.

13  
14 The sudden-limit analysis of section 3 assumes a single state (the  $1^2\Sigma^-$  state) is optically prepared  
15  
16 in the Franck-Condon region of the OH molecule. Lee<sup>15</sup> has argued that in the high-energy region  
17  
18 between the first and second dissociation thresholds of OH that predissociative levels of the  $A^2\Sigma^-$   
19  
20 ( $v' \geq 7$ ) state can also be accessed from the  $v''=0$  level of the ground state, and interference from the  
21  
22 predissociative and direct dissociation pathways could cause a strong local variation in the  $O(^3P_j)$  fine  
23  
24 structure branching ratios. By tuning the dissociation laser wavelength, the desired  $O(^3P_j)$  product  
25  
26 atom can then be selected in a type of internal coherent control method. In our experiment  
27  
28 excitation takes place from OH  $X(N''=1, J''=3/2, v''=0-5)$  at the dissociation wavelengths 243, 226, 205,  
29  
30 and 200 nm. A number of  $A^2\Sigma^-$  ( $v' \geq 7$ ) states lie in the 243-200 nm region when starting from  $X$   
31  
32 ( $v''=0-4$ ), but none are close to resonance with the specific O, H, or D atom REMPI lines we employ.  
33  
34 Excitation beginning from higher vibrational levels of the  $X$  state probes progressively larger  
35  
36 internuclear distances, which favors excitation to the repulsive  $1^2\Sigma^-$  state over excitation to bound  
37  
38 levels of the  $A^2\Sigma^-$  state. To produce the predicted branching ratio variations, the contributions from  
39  
40 the two indistinguishable dissociation pathways should be roughly comparable. We believe that  
41  
42 excitation to bound levels of the  $A^2\Sigma^-$  state is extremely weak at our photodissociation wavelengths  
43  
44 so that the photodissociation dynamics is reduced to that on the single  $1^2\Sigma^-$  state. Zhou et al.<sup>10</sup>  
45  
46 come to a similar conclusion in an investigation of the photodissociation dynamics of the isovalent  
47  
48 SH molecule.  
49  
50  
51  
52  
53  
54  
55  
56  
57  
58  
59  
60

Formatted: Superscript

Deleted: <sup>15</sup>

Deleted: <sup>10</sup>

Formatted: Complex Script Font:  
Bold, Superscript

1  
2 Lee also found that at energies above the second dissociation limit producing  $H(^2S) + O(^1D)$ , the  
3  
4 nonadiabatic (spin-orbit and Coriolis) couplings among electronic states correlating to  $O(^3P)$  are very  
5  
6 small compared with the kinetic energies of the  $O(^3P)$  fragments, and because of that their effects on  
7  
8 the dissociation to  $O(^3P)$  are expected to be minimal<sup>47</sup>. Lee found that the anisotropy parameters  
9  
10 for  $O(^3P)$  produced by photodissociation above the second dissociation limit are nearly energy-  
11  
12 independent, and very close to  $-1$ , and that the  $O(^3P)$  fine structure branching ratios are also very  
13  
14 similar to the recoil limit values in this energy regime.

15  
16 Zhou *et al.*<sup>10</sup> studied the photodissociation dynamics of jet-cooled SH in the photolysis  
17  
18 wavelength region of 216 to 232 nm using the high- $n$  Rydberg atom time of flight technique. Their  
19  
20 results also indicate that UV photolysis of SH is a due to one photon-direct dissociation of SH to the  
21  
22 dissociative  $1^2\Sigma^-$  curve from the ground state of SH ( $X^2\Pi, v''=0-2$ ). Their product fine structure states  
23  
24 distributions also showed that the  $S(^3P)$  spin-orbit branching fractions of SH are close to the 5:3:1  
25  
26 sudden limit distribution from the single  $1^2\Sigma^-$  state, as in the case of OH. Their experimental  $\beta$   
27  
28 parameters for the three spin-orbit products  $S(^3P)$  have the same  $\sim -1$  value in the 216–232 nm  
29  
30 region, which is similar to the results from this present study (for  $O(^3P_0)$  and  $D(^2S)$ ) where the  
31  
32 anisotropy parameters are also nearly energy-independent. We should also point out that our  
33  
34 uncertainties in branching ratios and angular distribution parameters are relatively large, due to the  
35  
36 very small populations of the vibrationally excited molecules studied in this work. Good agreement is  
37  
38 found for the sudden limit predictions, but it would still be worthwhile to use a different  
39  
40 experimental approach (such as VUV photodissociation) in order to obtain a higher experimental  
41  
42 precision for a more stringent comparison with theory.

Formatted: Complex Script Font:  
Italic, Superscript

Deleted: <sup>10</sup>

## 43 44 45 46 47 **7. CONCLUSION** 48 49 50 51 52 53 54 55 56 57 58 59 60

1  
2 While the photodissociation of OH/OD is energetically allowed above 4.37 eV ( $\lambda < 284$  nm),  
3  
4 Franck-Condon overlap restricts absorption from the X ground state  $v''=0$  to  $\lambda < \sim 180$  nm. When OH  
5  
6 is populated in higher vibrational levels, however, UV radiation can excite the molecules into the  
7  
8 direct dissociation  $1^2\Sigma^-$  continuum, leading to the observed H/D and O atom product signals. An  
9  
10 estimate of  $\sim 2000$ K for the vibrational temperature of the pulsed discharge beam source of OH was  
11  
12 obtained by comparing the relative signal levels from photodissociation from different vibrational  
13  
14 levels with theoretical predictions of the absorption cross section. The fragment angular  
15  
16 distributions for the D( $^2S$ ) and O( $^3P_0$ ) fragments, which are not complicated by atomic angular  
17  
18 momentum alignment effects, indicate a pure perpendicular molecular dissociation, as expected for  
19  
20 a  $1^2\Sigma^- \leftarrow X^2\Pi$  dissociation process. The measured O( $^3P_j$ ) product branching ratios are constant,  
21  
22 within our error limits, for the dissociation wavelengths 243 nm, 226 nm, 205 nm, and 200 nm, with  
23  
24 a  $\sim 5:3:1$  ratio for  $J = 2:1:0$ , as predicted theoretically for a sudden limit diabatic dissociation process.  
25  
26 In the sudden limit the  $M_j$  distribution for a given  $J$  state is quite non-statistical, and this introduces a  
27  
28 strong angle-dependent probability for ionization by the linearly polarized probe laser. The  
29  
30 measured angular distribution parameters  $\beta$  and  $\gamma$  for the O( $^3P_{2,1}$ ) product atoms are predicted  
31  
32 reasonably accurately by the sudden limit theoretical treatment. The values for these angular  
33  
34 distribution parameters are, like the O( $^3P_j$ ) branching ratios, independent of dissociation wavelength,  
35  
36 which is to be expected for photodissociation in the sudden limit regime. Experimental  
37  
38 complications such as ion-recoil from the photoionization step and possible OH pre-orientation and  
39  
40 alignment due to the hexapole focusing method were also discussed.

#### 41 42 43 44 **ACKNOWLEDGMENTS**

45  
46  
47  
48  
49 This work is part of the research program of the "Stichting voor Fundamenteel Onderzoek der  
50  
51 Materie (FOM)," which is financially supported by the "Nederlandse Organisatie voor  
52  
53  
54  
55  
56  
57  
58  
59  
60

1  
2  
3  
4  
5  
6  
7  
8  
9  
10  
11  
12  
13  
14  
15  
16  
17  
18  
19  
20  
21  
22  
23  
24  
25  
26  
27  
28  
29  
30  
31  
32  
33  
34  
35  
36  
37  
38  
39  
40  
41  
42  
43  
44  
45  
46  
47  
48  
49  
50  
51  
52  
53  
54  
55  
56  
57  
58  
59  
60

Wetenschappelijk Onderzoek (NWO).” The *ab initio* work has been financially supported by the Council for Chemical Sciences of the Netherlands Organization for Scientific Research (CW-NWO).

For Peer Review Only

## FIGURE CAPTIONS

**Figure 1:** Potential energy diagram of the OH electronic states relevant for this study. On the left side of the figure are photodissociation cross sections for excitation from the vibrational levels  $v'' = 0, 2$  and  $3$  of the ground ( $X^2\Pi$ ) electronic state to the repulsive  $1^2\Sigma^-$  state of OH from 100 to 350 nm. The vertical arrows represent one-photon dissociation at  $\sim 200$  nm of the repulsive  $1^2\Sigma^-$  state from the vibrational levels  $v''=2$  and  $3$  of the ground state of OH. At 200nm, for example, the photodissociation cross section from  $v''=2$  is larger than that from  $v''=3$ .

**Figure 2:** Raw  $O^+$  images produced by one-photon photodissociation of: (a) OH and (b) OD. The  $O(2p^3P_j)$  ( $J=2,1,0$ ) atoms were ionized by (2+1) REMPI through the  $O(3p^3P_j)$  states (images a) and b)) at  $\sim 226$  nm, and by (2+1) REMPI through the  $O(4p^3P_j)$  states (images a') and b')) at  $\sim 200$  nm. Raw images of  $D^+$  from the one photon dissociation of OD formed from  $D(1s^2S)$  atoms by (2+1) REMPI through the: (c)  $D(2s^2S)$  state at the wavelength 243.09 nm and (c')  $D(3s^2S)$  states at 205.07 nm. A grayscale bar (left side) shows the relative signal intensity, where the darker areas correspond to higher signal. The dot in the center of each image corresponds to zero-velocity fragment  $O(^3P_j)$  or  $D(^2S)$  atoms formed in the discharge source. The outer rings originate from photodissociation of vibrationally excited OH/OD  $X^2\Pi$  radicals. The vertical arrow ( $\updownarrow$ ) indicates the direction of the laser polarization.

**Figure 3:** Abel inverted images of: (a)  $O(^3P_2)$ , (b)  $D(^2S)$  formed from the one photon dissociation of vibrationally excited OD  $X^2\Pi$  radicals at  $\sim 200$  and  $\sim 205$  nm, respectively. On the left side a intensity grey-scale is presented. On the right side the vertical arrow ( $\updownarrow$ ) presenting the laser polarization. The  $O^3P$  image is smaller than the D image, it has been scaled to the same size for comparison. Note that the weak extra inner rings in the  $O^3P$  images for OD come from an OH impurity.

**Figure 4:** Total kinetic energy release (TKER) distribution for the images shown in Figure 3. The initial vibrational state of OD is determined from energy balance with  $TKER = hv + E(vib)OD - D_0(OD)$ . The bar graphs show the calculated photodissociation yields for OD  $X^2\Pi$  ( $v$ ) at a vibrational temperature of 2000 K.

1  
2 **Figure 5:** Abel inverted images of  $O(^3P_2)$  formed from the one photon dissociation of vibrationally excited  $OH X^2\Pi$   
3 radicals at: (a)  $\sim 226$  and (b)  $\sim 200$  nm, respectively( rescaled to same size). See figure caption 2 for other details.  
4

5  
6 **Figure 6:** Total kinetic energy release (TKER) distribution for the images shown in Figure 5. The initial vibrational state  
7 of OH is determined from energy balance with  $TKER = hv + E(vib)_{OH} - D_0(OH)$ . The bar graphs show the calculated  
8 photodissociation yields for  $OH X^2\Pi (v)$  at a vibrational temperature of 2000 K.  
9

10  
11 **Figure 7:** The measured angular distribution and fitted curves for the strongest peaks of the dissociation  
12 products  $O(^3P_{2,1,0})$  coming from one photon dissociation of: a) OH at  $\sim 226$  (upper panel) and  $\sim 200$  nm (lower  
13 panel); b) OD at  $\sim 226$  (upper panel) and  $\sim 200$  nm (lower panel) and c) The measured angular distribution and  
14 fitted curves for the strongest peaks of the dissociation products  $D(^2S)$  coming from one photon dissociation  
15 of: OD at  $\sim 243$  and  $\sim 205$  nm, respectively. The angular distribution is fit to the expression:  $I(\theta) = 1 + \beta P_2(\cos \theta)$   
16  $+ \gamma P_4(\cos \theta)$ .  
17  
18  
19  
20  
21

22  
23 **Figure 8:** Experimental  $\beta$  and  $\gamma$  values plotted as a function of wavelength ( $\sim 226$  and  $\sim 200$  nm)  
24 corresponding to the different fine structure states of the  $O(^3P_J)$  atom ( $J=2,1,0$ ) from photodissociation of OH  
25 and OD.  $\beta$  and  $\gamma$  with experimental error bars are represented by a filled square for OH and by a filled triangle  
26 for OD. Calculated anisotropy parameters  $\beta$  and  $\gamma$  in the sudden-recoil limit, characterizing the angular  
27 distribution of  $O(^3P_J)$  (with  $J=2,1,0$ ) photofragments formed in the one photon process photodissociation of  
28 OH/OD via the  $1^2\Sigma^-$  state are represented by a hollow square.  
29  
30  
31  
32  
33

34  
35 **Figure 9:** The Doppler- free (a) and corresponding Abel inverted image (b) of  $D(^2S)$  formed from the one  
36 photon dissociation of vibrationally excited  $OD X^2\Pi$  radicals at  $\sim 243$  nm. See figure 3 for other details.  
37  
38  
39  
40  
41  
42  
43  
44  
45  
46  
47  
48  
49  
50  
51  
52  
53  
54  
55  
56  
57  
58  
59  
60

**TABLES and CAPTIONS**Table I: The sudden recoil limit for the OH  $X(2\Pi) + hv \rightarrow 12\Sigma^- \rightarrow H(2S) + O(3P_J)$  direct dissociation.Columns 3-5 give the populations  $p_J\omega$ . The symbols are defined in Sec. 3.2.

J	$p_J$	$\omega$			$r_J$	$\beta_J$	$\gamma_J$
		0	1	2			
0	1/9	1/9			1/8	-1	
1	1/3	0	1/6		$1/\sqrt{2}$	-5/7	-2/7
2	5/9	2/9	1/6	0	$-\sqrt{2}$	-25/43	-18/43

Deleted: 2

Deleted: ~~~~~Page Break~~~~~  
¶

**Table 2.** Experimentally observed and calculated fragment recoil velocity, velocity uncertainty, kinetic energy and ion-recoil velocity for photodissociation of OH and OD at 243, 226, 205, and 200 nm.

Parent	Frag.	$\lambda_{\text{diss}}$ (nm)	Assign.	TKER (eV)	$v_{\text{calc.}}$ (m/s)	$v_{\text{meas.}}$ (m/s)	$\Delta v$ (m/s)	spacing (m/s)	$v_{\text{recoil}}$ (m/s)
OH	$\text{O}(^3\text{P}_J)$	226	$v''=2$	2.02	1173	1200	20	117	35
			$v''=3$	2.39	1290	1300			
OD	$\text{O}(^3\text{P}_J)$	226	$v''=3$	2.08	1622	1670	35	118	35
			$v''=4$	2.32	1740	1765			
OH	$\text{O}(^3\text{P}_J)$	200	$v''=1$	2.23	1252	1250	20	115 98	45
			$v''=2$	2.60	1367	1345			
			$v''=3$	3.08	1465	1475			
OD	$\text{O}(^3\text{P}_J)$	200	$v''=2$	2.34	1774	1770	20	109 103	45
			$v''=3$	2.64	1883	1870			
			$v''=4$	2.98	1986	1995			
OD	$\text{D}(^2\text{S})$	243	$v''=2$	1.33	10420	10680	220	1185 1040	212
			$v''=3$	1.56	11605	11555			
			$v''=4$	1.80	12650	12430			
OD	$\text{D}(^2\text{S})$	205	$v''=1$	1.80	12745	12425	230	920 835	347
			$v''=2$	2.16	13765	13610			
			$v''=3$	2.44	14685	14470			

**Table 3.** Experimentally observed  $O(^3P)$ ,  $J=2,1,0$  branching ratios (uncertainty 0.05) from the photodissociation of OH and OD at 226 and 200 nm.

		Branching ratio		
		J=2	J=1	J=0
~226 nm	OH	0.59	0.30	0.11
	OD	0.51	0.35	0.14
~200 nm	OH	0.55	0.33	0.13
	OD	0.49	0.35	0.16

Table 4. Top) Experimentally determined anisotropy parameters  $\beta_{\text{exp}}$  and  $\gamma_{\text{exp}}$  extracted for the strongest peaks seen in the background subtracted and fine structure state selected  $O^+$  images for one-photon dissociation of OH/OD at  $\sim 226$  and  $\sim 200$  nm. Middle) the corresponding anisotropy parameters  $\beta_{\text{calc.}}$  and  $\gamma_{\text{calc.}}$  predicted theoretically, using the sudden limit analysis. Lower) Experimentally determined anisotropy parameters  $\beta_{\text{exp}}$  extracted for the strongest peaks seen in the observed background subtracted  $D^+$  images coming from one-photon photodissociation of OD at  $\sim 243$  and  $\sim 205$  nm and anisotropy parameters  $\beta$  extracted for the strongest peaks seen in the Doppler free  $D^+$  image from one photon photodissociation of OD at  $\sim 243$  nm. The estimated uncertainty of  $\beta$  and  $\gamma$  is 0.1. Values of the uncertainties in  $\beta$  and  $\gamma$  which are larger than 0.1 are indicated in the table.

Transition		$O(^3P_2)$		$O(^3P_1)$		$O(^3P_0)$	
		$\beta_{\text{exp}}$	$\gamma_{\text{exp}}$	$\beta_{\text{exp}}$	$\gamma_{\text{exp}}$	$\beta_{\text{exp}}$	$\gamma_{\text{exp}}$
$\sim 226$ nm	OH ( $v''=2$ )	-0.44	-0.23	-0.74	-0.10	-0.86	+0.08
	OD ( $v''=3$ )	-0.56	-0.20	-0.64	+0.03	-0.82	-0.05
$\sim 200$ nm	OH ( $v''=1$ )	-0.52	-0.43(15)	-0.65	-0.31(19)	-0.94(51)	-0.96(70)
	OD ( $v''=2$ )	-0.61(16)	-0.27(22)	-0.67(18)	-0.09(23)	-0.99(65)	+0.26(87)

Sudden limit analysis		$O(^3P_2)$		$O(^3P_1)$		$O(^3P_0)$	
		$\beta_{\text{calc.}}$	$\gamma_{\text{calc.}}$	$\beta_{\text{calc.}}$	$\gamma_{\text{calc.}}$	$\beta_{\text{calc.}}$	$\gamma_{\text{calc.}}$
		-0.58	-0.42	-0.71	-0.28	-1	0

			$D(^2S)$
			$\sim 243$ nm
		$\beta$	-1.02
$\sim 205$ nm	OD ( $v''=2$ )	$\beta_{\text{exp}}$	-1.00

**REFERENCES**

- 
- <sup>1</sup> D. Č. Radenović, A. J. A. Van Rooij, D. A. Chestakov, A. T. J. B. Eppink, J. J. ter Meulen, D. H. Parker, M. P. J. Van der Loo, G. C. Groenenboom, M. E. Greenslade, and M. I. Lester, *J. Chem. Phys.* **119**, 9341 (2003).
- <sup>2</sup> W. Zhou, Y. Yuan, and J. Zhang, *J. Chem. Phys.* **119**, 9989(2003)
- <sup>3</sup> M. C. Abrams, S. P. Davis, M. L. P. Rao, and R. Engleman, Jr., *J. Mol. Spectrosc.* **165**, 57 (1994).
- <sup>4</sup> E. F. Dishoeck and A. Dalgarno, *J. Chem. Phys.* **79**, 873 (1983).
- <sup>5</sup> W. G. Roberge, A. Dalgarno, and B. P. Flannery, *Astrophys. J.* **243**, 817 (1981).
- <sup>6</sup> E. F. van Dishoeck, S. R. Langhoff, and A. Dalgarno, *J. Chem. Phys.* **78**, 4552 (1983).
- <sup>7</sup> M. C. van Beek and J. J. ter Meulen, *Chem. Phys. Lett.* **337**, 237(2001).
- <sup>8</sup> A. T. J. B. Eppink and D. H. Parker, *Rev. Sci. Instrum.* **68**, 3477(1997).
- <sup>9</sup> L. M. C. Janssen, M. P. J. van der Loo, G. C. Groenenboom, S.-M. Wu, D. C. Radenovic, A. J. A. van Rooij, I. A. Garcia, and D. H. Parker, *J. Chem. Phys.* **126**, 094304 (2007).
- <sup>10</sup> W. Zhou, Y. Yuan, S. Chen, and J. Zhang, *J. Phys. Chem.* **128**, 054330 (2005).

1  
2  
3  
4  
5 <sup>11</sup> M. P. J. Van der Loo and G. C. Groenenboom, J. Chem. Phys., **123**, 074310 (2005).  
6  
7

8 <sup>12</sup> G. H. Dieke and H. M. Crosswhite, J. Quant. Radiat. Transfer **2**, 97 (1962)  
9

10 <sup>13</sup> D. R. Yarkony, J. Chem. Phys. **97**, 1838 (1992).  
11  
12

13 <sup>14</sup> C. Kalyanaraman and N. Sathyamurthy, Chem. Phys. **187**, 219 (1994).  
14  
15

16 <sup>15</sup> S. Y. Lee, J. Chem. Phys. **103**, 3501 (1995).  
17  
18

19 <sup>16</sup> M.E. Greenslade, M. I. Lester, D. Č. Radenović, A. J. A. van Roij and D. H. Parker,  
20  
21

J. Chem. Phys. **123** (2005) 074309.  
22  
23

24 <sup>17</sup> MOLPRO is a package of *ab initio* programs written by H.-J. Werner and  
25  
26

P. J. Knowles, with contributions from R. D. Amos, A. Berning, D. L. Cooper,  
27  
28

M. J. O. Deegan, A. J. Dobbyn, F. Eckert, C. Hampel, T. Leininger, R. Lindh,  
29  
30

W. Lloyd, W. Meyer, M. E. Mura, A. Nicklaß, P. Palmieri, K. Peterson, R. Pitzer,  
31  
32

P. Pulay, G. Rauhut, M. Schutz, H. Stoll, A. J. Stone and T. Thorsteinsson  
33  
34  
35  
36  
37

38 <sup>18</sup> P. J. Knowles and H.-J. Werner, Chem. Phys. Lett. **145**, 514 (1988).  
39  
40

41 <sup>19</sup> H.-J. Werner and P. J. Knowles, J. Chem. Phys. **89**, 5803 (1988).  
42  
43

44 <sup>20</sup> H.-J. Werner and P. J. Knowles, J. Chem. Phys. **82**, 5053 (1985).  
45  
46

47 <sup>21</sup> P. J. Knowles and H.-J. Werner, Chem. Phys. Lett. **115**, 259 (1985).  
48  
49

50 <sup>22</sup> D. T. Colbert and W. H. Miller, J. Chem. Phys. **96**, 1982 (1992).  
51  
52  
53  
54  
55  
56  
57  
58  
59  
60

- 1  
2  
3  
4  
5 <sup>23</sup> G. C. Groenenboom and D. T. Colbert, *J. Chem. Phys.* **99**, 9681 (1993).  
6  
7  
8 <sup>24</sup> J. B. Lee and L. C. Nee *J. Chem. Phys.* **81**, 31 (1984).  
9  
10 <sup>25</sup> M. C. G. N. van Vroonhoven and G. C. Groenenboom, *J. Chem. Phys.*, 116, 1965 (2002).  
11  
12  
13 <sup>26</sup> Y. Mo, H. Katayanagi, M. C. Heaven, and T. Suzuki, *Phys. Rev. Lett.* **77**, 830 (1996).  
14  
15  
16  
17 <sup>27</sup> S. J. Singer, K. F. Freed, and Y. B. Band, *J. Chem. Phys.* **79**, 6060 (1983).  
18  
19  
20 <sup>28</sup> K. Schreel and J. J. ter Meulen, *J. Phys. Chem. A* **101**, 7639 (1997).  
21  
22  
23 <sup>29</sup> J. Luque and D. R. Crosley, "LIFBASE: Database and Spectral Simulation  
24 Program (Version 1.5)," SRI International Report No. MP 99-009 (1999).  
25  
26  
27  
28 <sup>30</sup> E. de Beer, M. P. Koopmans, C. A. De Lange, Y. Wang, and W. A. Chupka,  
29  
30 *J. Chem. Phys.* **94**, 7634 (1991).  
31  
32  
33 <sup>31</sup> A. M. Coroiu, D. H. Parker, G. C. Groenenboom, J. Barr, I. T. Novalbos and B. J. Whitaker, *Eur.*  
34 *Journal Physics D*, **38**, 151 (2006).  
35  
36  
37 <sup>32</sup> V. Dribinski, A. Ossadtchi, V.A. Mandelshtam, H. Reisler, *Rev. Sci. Instrum.* **73**, 2634 (2002).  
38  
39  
40 <sup>33</sup> C. Carlone and F. Dalby, *Can. J. Phys.* **47**, 1945 (1969).  
41  
42  
43 <sup>34</sup> B. Ruscic, D. Feller, D. A. Dixon, K. A. Peterson, L. B. Harding,  
44  
45 R. L. Asher, and A. F. Wagner, *J. Phys. Chem. A* **105**, 1(2001).  
46  
47  
48 <sup>35</sup> M. Cacciatore, M. Capitelli, S. De Benedictis, M. Dilonardo, and C. Gorse, *Topics*  
49  
50  
51  
52  
53  
54  
55  
56  
57  
58  
59  
60

in *Current Physics* **39**, 5 (1986); M. Capitelli, C. Gorse, and A. Ricard, *ibid.* **39**,

315 (1986).

<sup>36</sup> J. Fleniken, Y. Kim and H. Meyer, *Chem. Phys. Lett.* **318**, 529 (2000).

<sup>37</sup> G. B. Courreges-Lacoste, J. P. Sprengers, J. Bulthuis, S. Stolte, T. Motylewski,

and H. Linnartz, *Chem. Phys. Lett.* **335**, 209 (2001).

<sup>38</sup> M. E. Sanz, M.C. McCarthy, and P. Thaddeus, *J. Chem. Phys.* **119**, 11715 (2003).

<sup>39</sup> D.H. Parker, R.F. Delmdahl, B.B.L.G. Bakker and H.P. Loock. *J. Chin. Chem. Soc.* **48** 327 (2001).

<sup>40</sup> S. Manzhos, H.-P. Loock, B.L.G. Bakker and D.H. Parker. *J. Chem. Phys.* **117**

(2002) 9347.

<sup>41</sup> R. L. Toomes, P. C. Samartzis, T. P. Rakitzis and T. N. Kitsopoulos *Chem. Phys.* **301**

(2004) 209.

<sup>42</sup> H. L. Offerhaus, C. Nicole, F. Lépine, C. Bordas, F. Rosca-Pruna and M. J. J. Vrakking, *Rev. Sci.*

*Instrum.* **72**, 3245 (2001).

<sup>43</sup> M. L. Lipciuc and M. H. M. Janssen, *Phys. Chem. Chem. Phys.*, **8**, 3007 (2006); D. A. Chestakov,

*M. Wu, G. Wu, A. T. J. B. Eppink, D. H. Parker and T. N. Kitsopolous, *J. Phys. Chem A*, **108**, 8100*

*(2004).*

<sup>44</sup> A. E. Pomerantz and R. N. Zare, *Chem. Phys. Lett.* **370**, 515(2003)

Formatted: Font: Calibri, 11 pt, Complex Script Font: 11 pt

Formatted: Font: Calibri, 11 pt, Bold, Complex Script Font: 11 pt

Formatted: Font: Calibri, 11 pt, Complex Script Font: 11 pt

Formatted: Font: 11 pt, Complex Script Font: 11 pt

Formatted: Font: 11 pt

Formatted: Normal, Don't adjust right indent when grid is defined, Don't adjust space between Latin and Asian text, Don't adjust space between Asian text and numbers

Formatted: English U.S.

Formatted: English U.S.

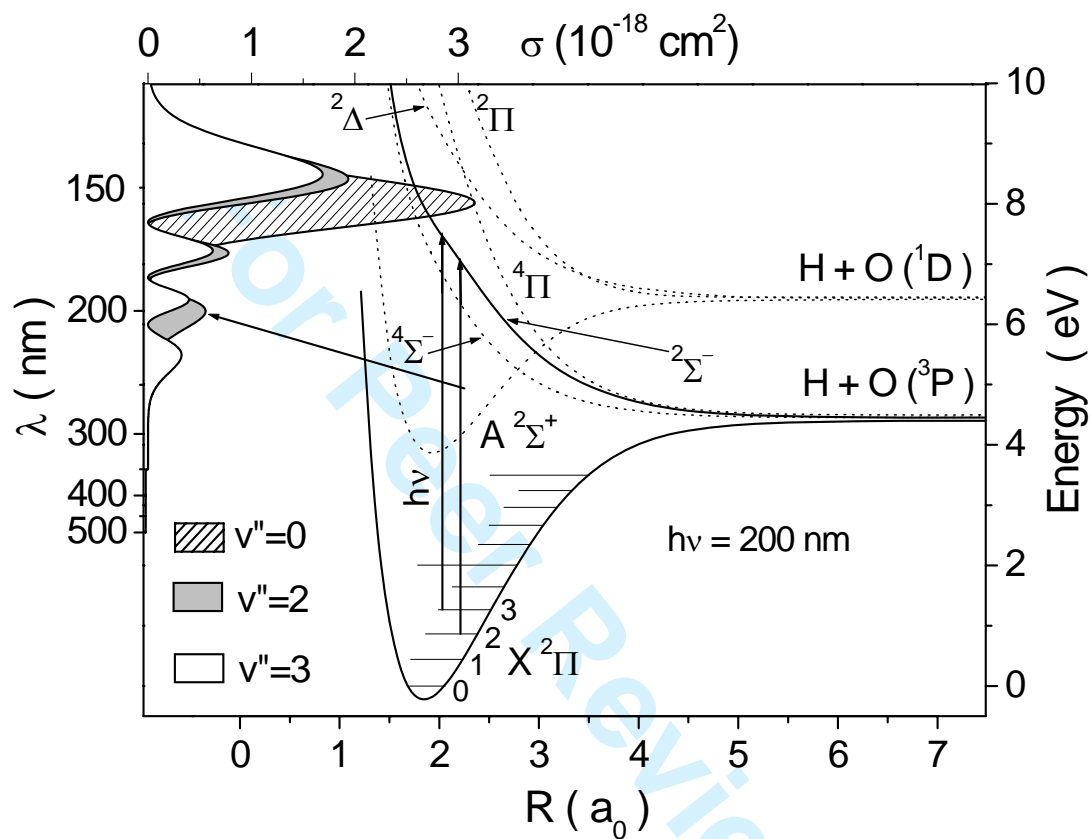
1  
2  
3  
4  
5  
6  
7  
8  
9  
10  
11  
12  
13  
14  
15  
16  
17  
18  
19  
20  
21  
22  
23  
24  
25  
26  
27  
28  
29  
30  
31  
32  
33  
34  
35  
36  
37  
38  
39  
40  
41  
42  
43  
44  
45  
46  
47  
48  
49  
50  
51  
52  
53  
54  
55  
56  
57  
58  
59  
60

<sup>45</sup> T. P. Rakitzis, A.J. van den Brom, M.H.M. Janssen, *Science* **303**, 1852 (2004).

<sup>46</sup> M. C. van Beek, J. J. ter Meulen and M.H. Alexander, *J. Chem. Phys.* **113**, 637 (2000).

<sup>47</sup> S. Y. Lee, *J. Chem. Phys.* **111**, 6407 (1999).

For Peer Review Only

Figure 1 Radenovic *et al.*

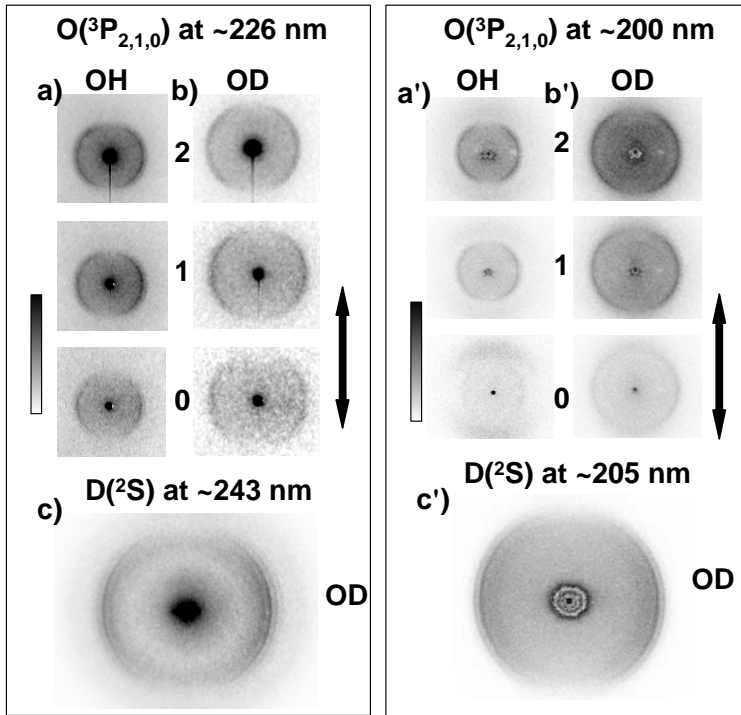


Fig. 2 Radenovic et al.

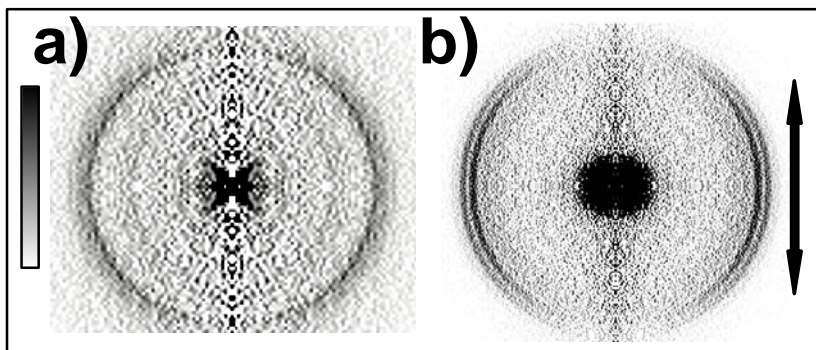


Figure 3 Radenovic et al.

For Peer Review Only

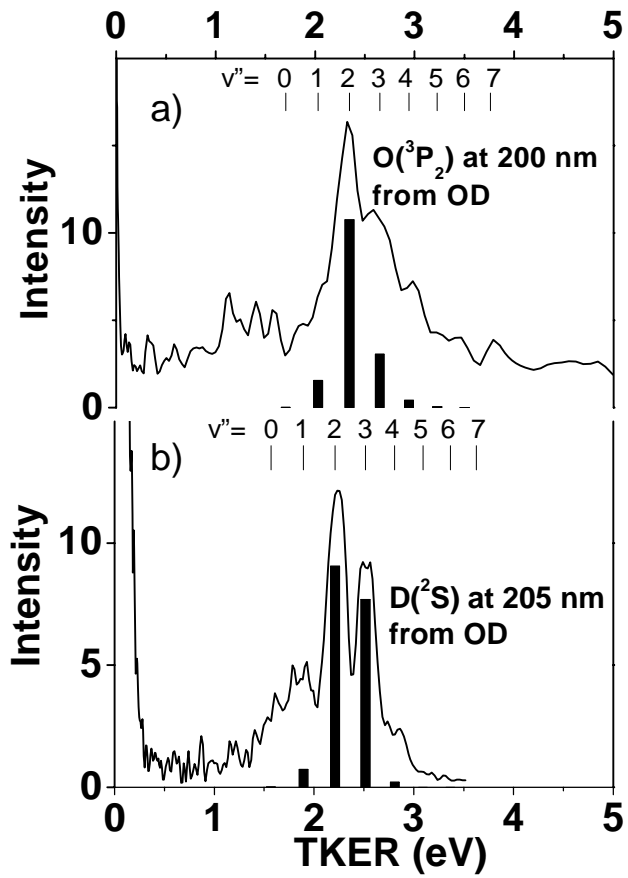


Figure 4. Radenovic et al.

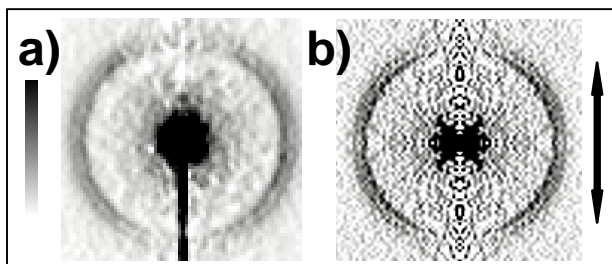


Figure 5 Radenovic et al.

For Peer Review Only

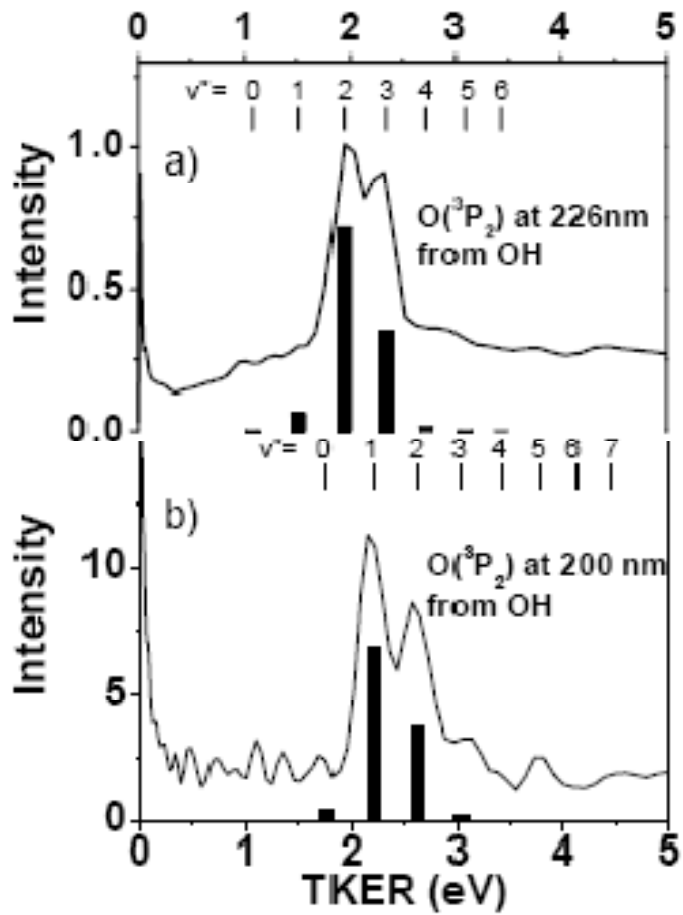


Figure 6. Radenovic et al.

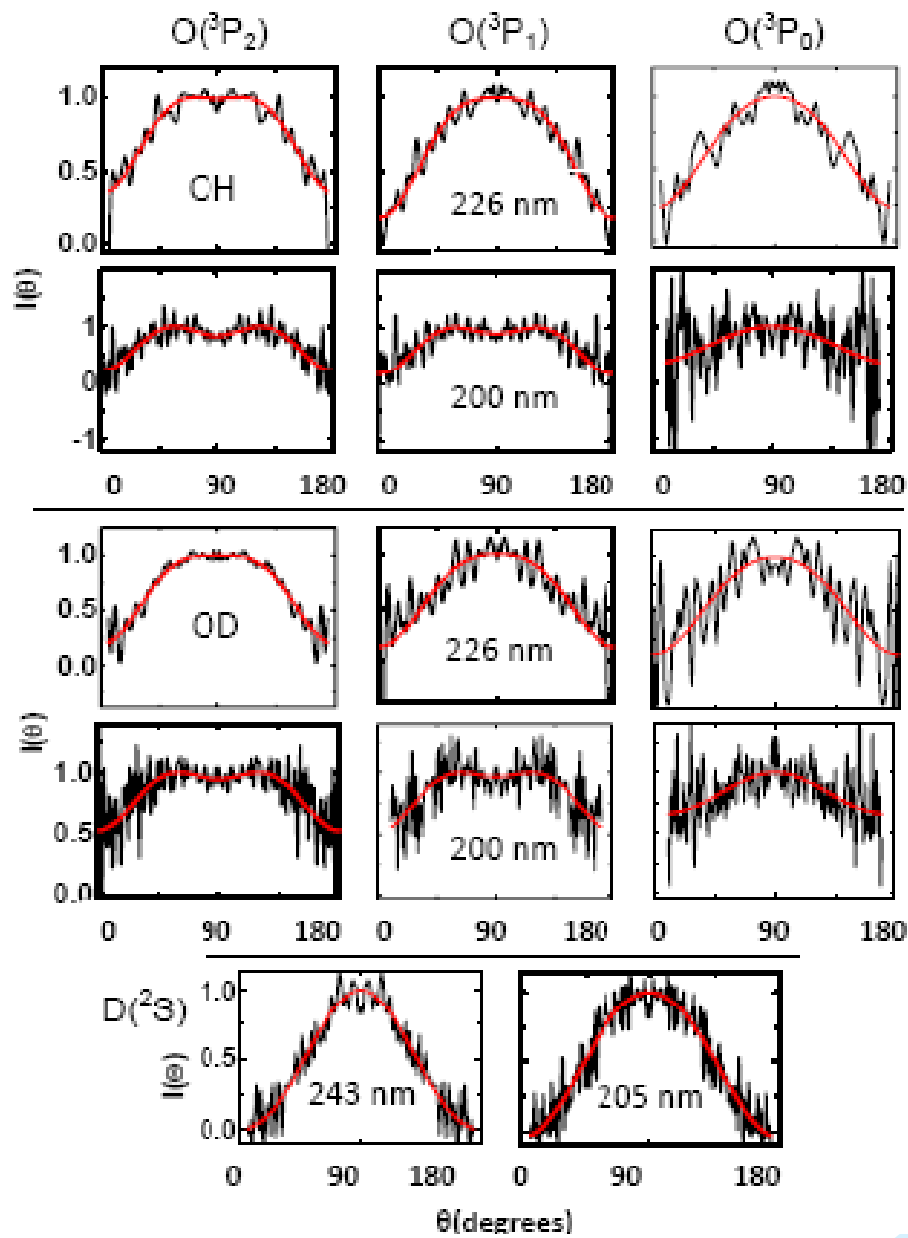


Figure 7. Radenovic et al.

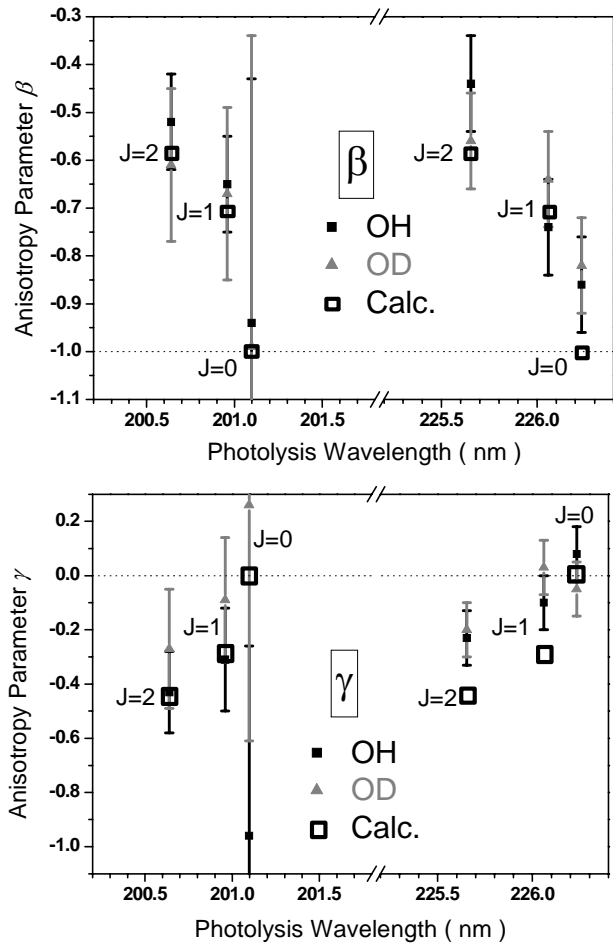


Figure 8. Radenovic et al.

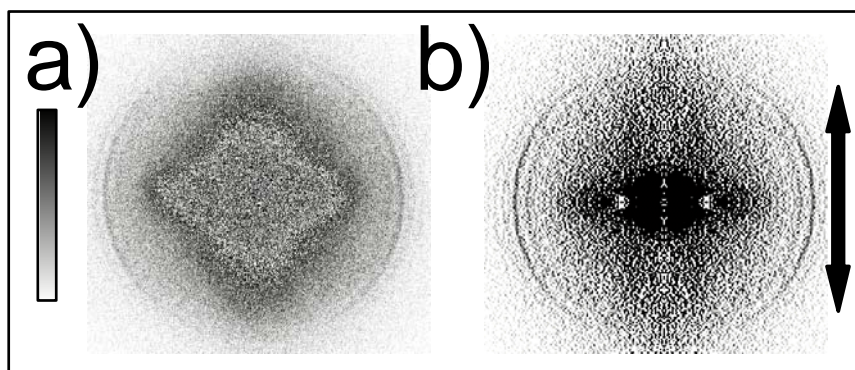
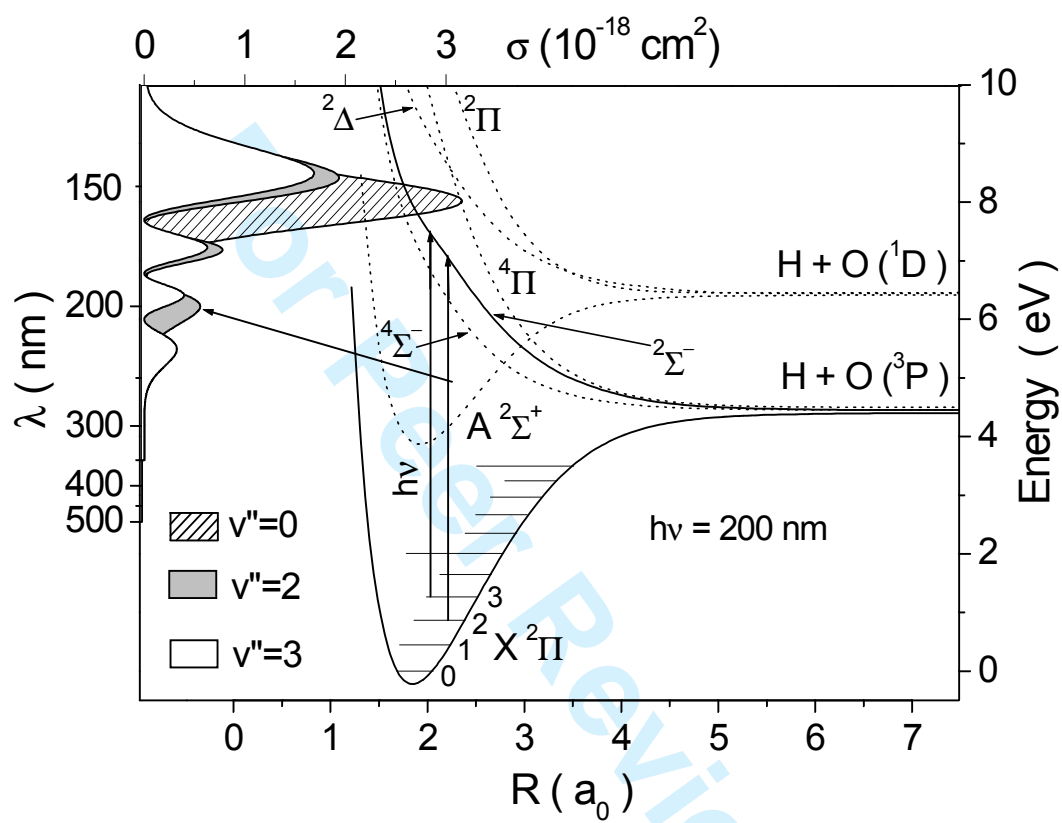


Figure 9. Radenovic et al.

Peer Review Only

1  
2  
3  
4  
5  
6  
7  
8  
9  
10  
11  
12  
13  
14  
15  
16  
17  
18  
19  
20  
21  
22  
23  
24  
25  
26  
27  
28  
29  
30  
31  
32  
33  
34  
35  
36  
37  
38  
39  
40  
41  
42  
43  
44  
45  
46  
47  
48  
49  
50  
51  
52  
53  
54  
55  
56  
57  
58  
59  
60

For Peer Review Only

Figure 1 Radenovic *et al.*

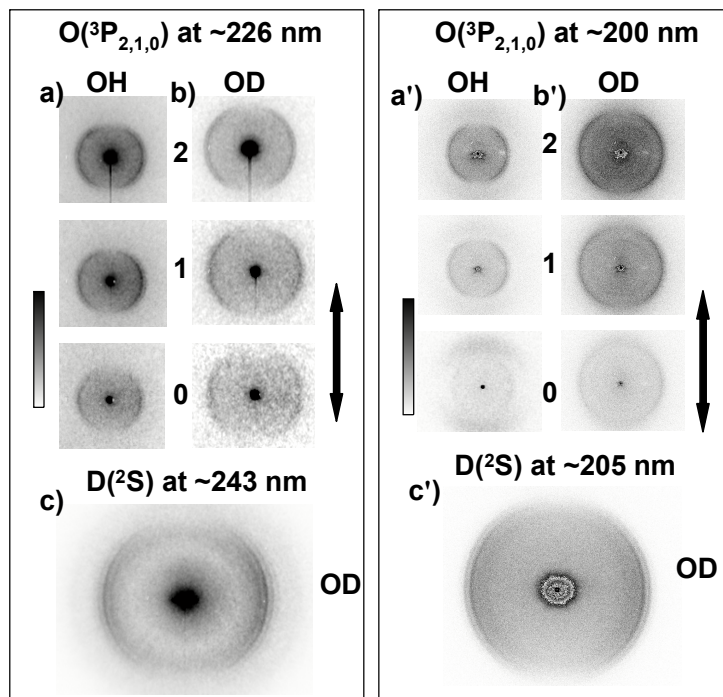


Fig. 2 Radenovic et al.

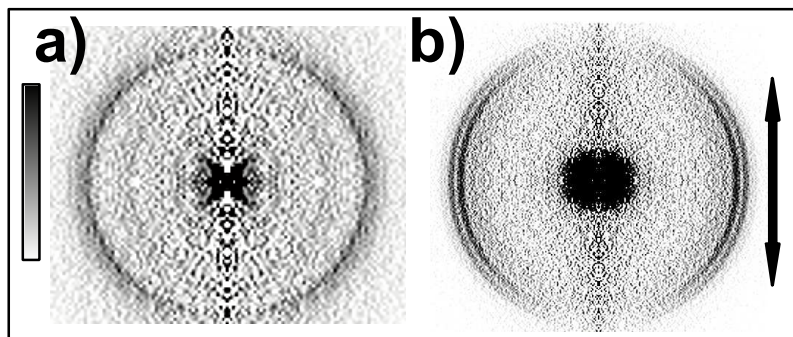


Figure 3 Radenovic et al.

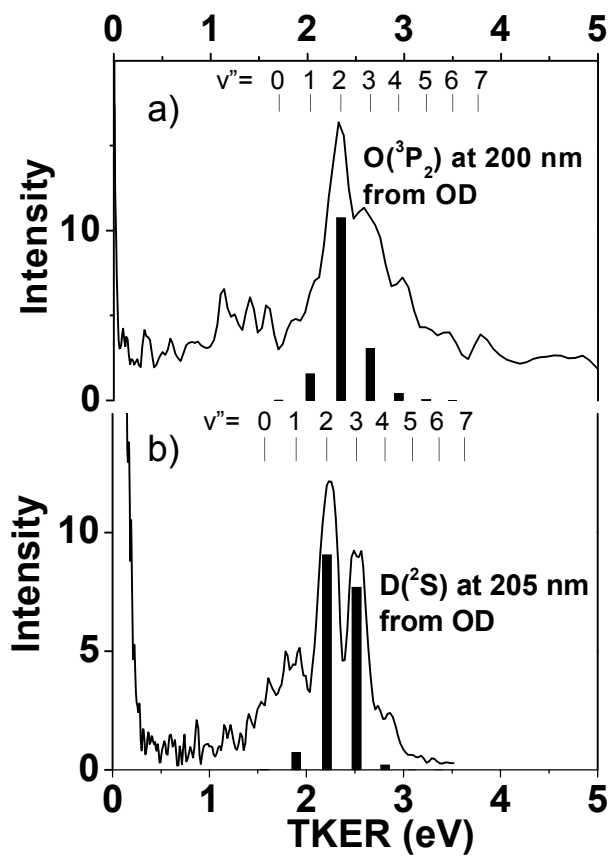


Figure 4. Radenovic et al.

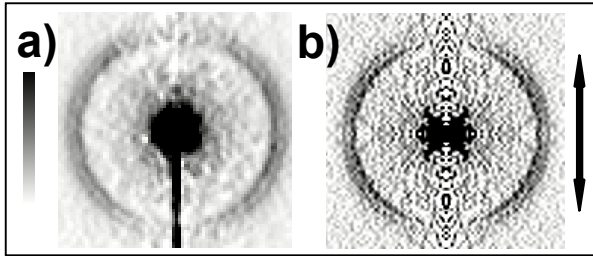


Figure 5 Radenovic et al.

or Peer Review Only

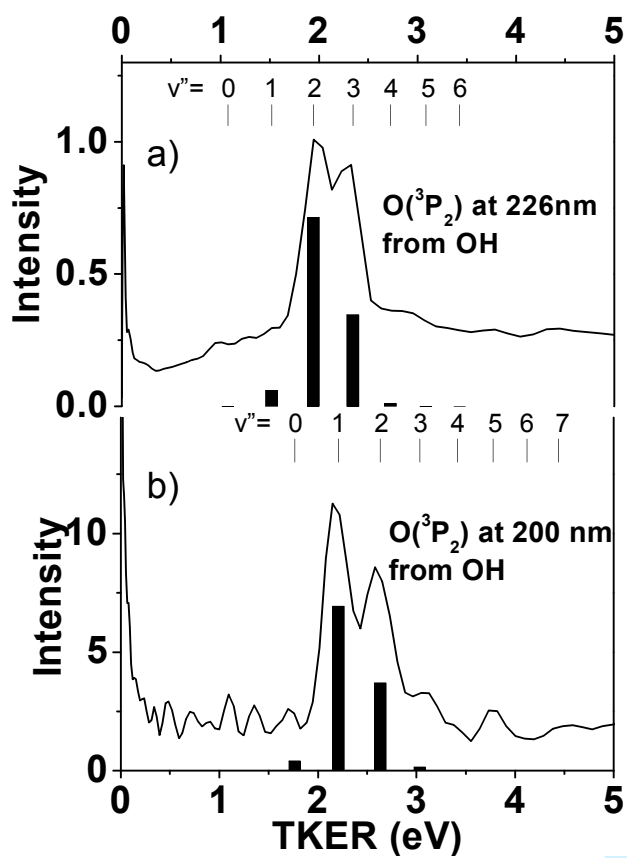


Figure 6. Radenovic et al.

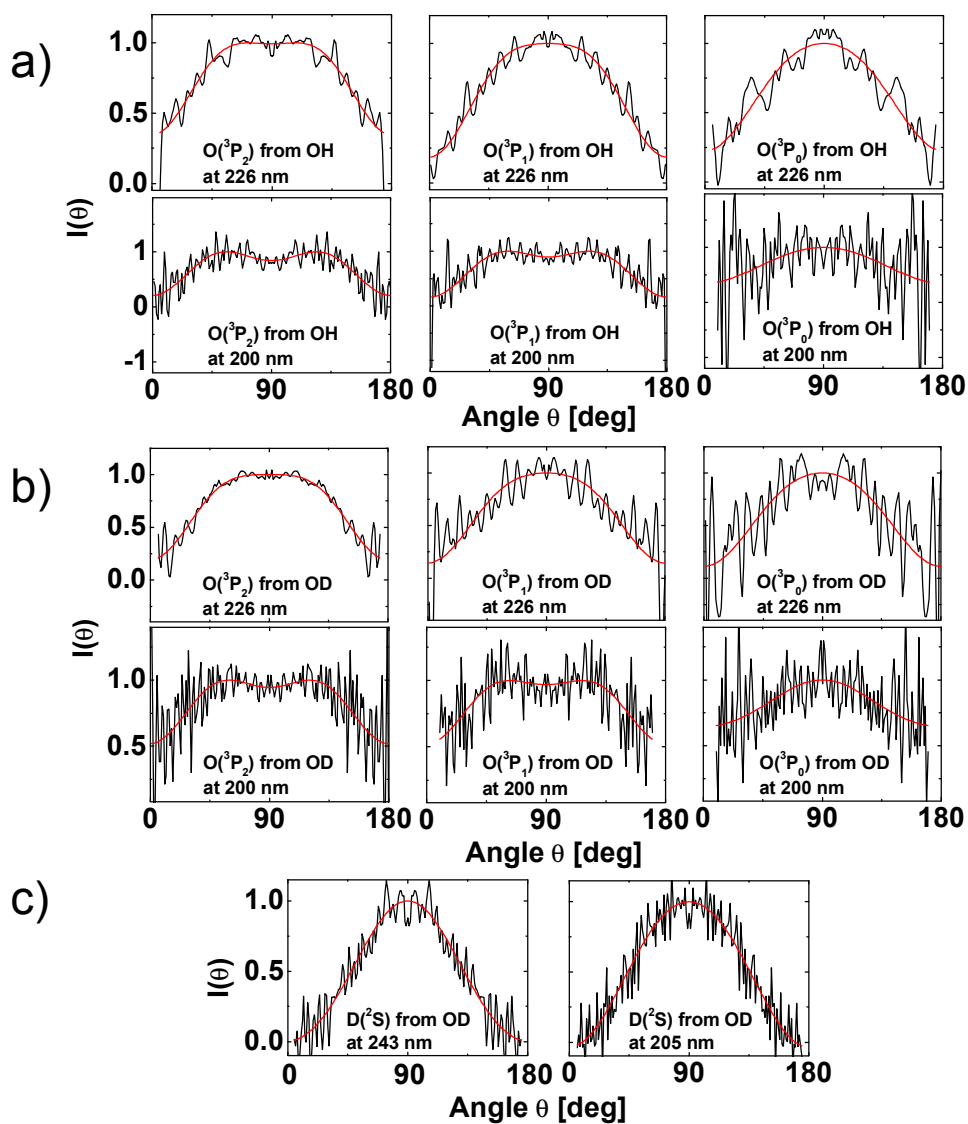


Figure 7. Radenovic et al.

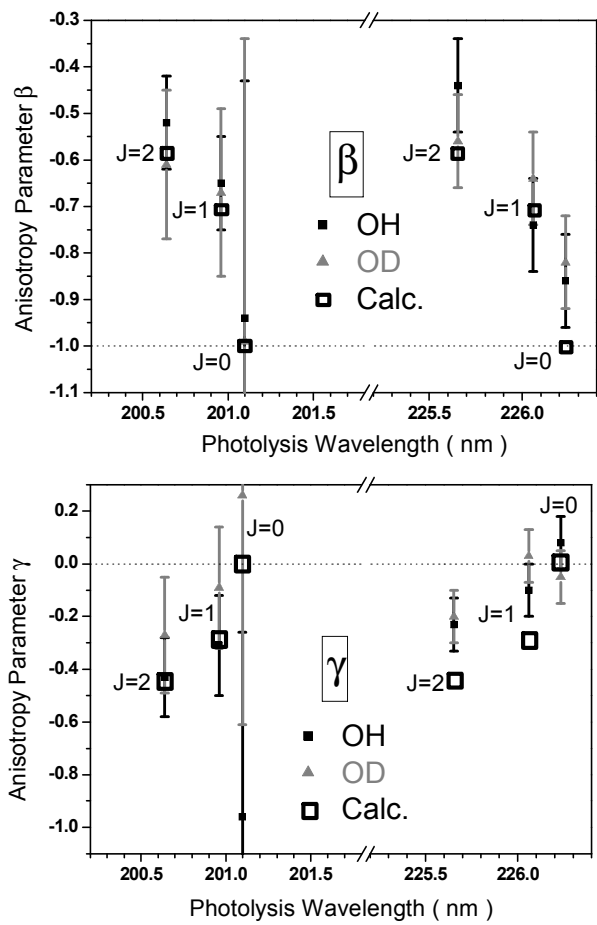


Figure 8. Radenovic et al.

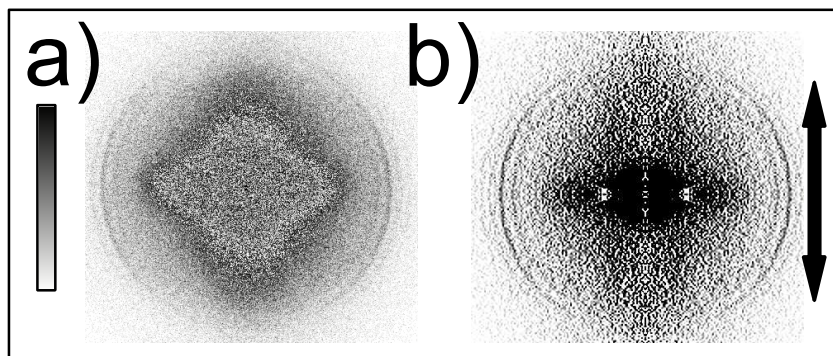


Figure 9. Radenovic et al.